2.8. Cell viability assay

For the cytotoxicity assay, PanC-1 cells (Pancreatic cancer cells, ATCC Number: CRL-1469) were seeded with 100 μL of DMEM containing 10% FBS in a 96 well plate (5000 cells/well) and incubated for 24 h. The nanoparticles (containing 10–1500 nM siRNA) were added with the fresh medium containing 10% FBS, and the cell viability was evaluated after 48-h incubation by Cell Counting Kit-8 (Dojindo, Kumamoto, Japan) according to the protocol provided by the manufacturer. Each well was measured by reading the absorbance at 450 nm in a Microplate Reader (Bio-Rad Model 680, Bio-Rad Laboratories, UK). The results were expressed as the percentage (%) of the control cells, which were incubated only with the culture medium.

2.9. Confocal laser scanning microscopy (CLSM) observation

PanC-1 cells were cultured with 1.5 mL of DMEM containing 10% FBS on 35-mm glass-base dishes (Iwaki, Japan) at 5×10^4 cells/dish. After 24 h, the medium was exchanged with fresh one and Cy5-labeled siRNA-containing nanoparticles were applied to the dish (100 nM siRNA). The nuclei and the endosome/lysosome were stained with Hoechst 33342 (Dojindo Laboratories, Kumamoto, Japan) for 5 min and LysoTracker Green (Molecular Probes, Eugene, OR) for 15 min before CLSM imaging, respectively. Cells were rinsed 3 times with PBS and fresh medium was added prior to the imaging. CLSM images were acquired at 3 and 24 h after nanoparticle administration, using a Zeiss LSM 510 META (Carl Zeiss, Germany) with a water-immersion 63× objective (C-Apochromat, Carl Zeiss). Excitation wavelengths were 488 nm (argon laser), 633 nm (He–Ne laser), and 710 nm (Mai Tai laser, operated in a two-photon mode) for LysoTracker, Cy5, and Hoechst 33342, respectively. The co-localization ratio was calculated as previously described [24] with the formula:

Co-localization ratio = number of yellow pixels/number of yellow and red pixels.

2.10. Real-time reverse transcription (RT)-PCR

PanC-1 cells were seeded with 2000 μL of DMEM containing 10% FBS on a 6 well plate at 8×10^4 cells/well. After 24 h, nanoparticles were added with fresh medium (60 nM siRNA). After 3 h of exposing the cells to nanoparticles, the medium was changed to fresh one. Twenty four hours later, cells were harvested and RNA was extracted using the RNeasy Mini Kit (Qiagen, Valencia, CA), according to the manufacturer's instruction. The amount of extracted RNA was measured and standardized after the genomic DNA elimination for the cDNA synthesis (QuantiTect Reverse Transcription, Quiagen, Valencia, CA). Real-time RT-PCR was performed using the ABI 7500 Fast Real-time RT-PCR System (Applied Biosystems, Foster City, CA) and QuantiTect SYBR Green PCR Master Mix (Qiagen, Valencia, CA). The actin was used as a house-keeper gene and the obtained data were normalized before statistical analysis.

2.11. Statistical analysis

The analysis of variance (ANOVA) was performed to test the treatment effects, and Bonferroni's test was used as *post hoc* pairwise comparisons between individual treatment groups, using the software GraphPad Prism 3.0 (GraphPad Software, Inc.). Statistical significance is represented as * for $p < 0.05$ and ** for $p < 0.01$. Unless indicated, all experiments were performed in triplicate ($N = 3$) and the results reported were expressed as mean values (±SEM).

3. Results and discussion

3.1. Synthesis of charge-conversional and non-charge-conversional polymers

The synthesis route of PEG-PAsp(DET-Aco) as a charge-conversional polyanion is illustrated in Scheme 1, as well as two polyanions used as controls without the charge-conversional property. PEG-PAsp(DET) was synthesized from PEG–PBLA (M_w of PEG 12,000; DP of PBLA 96) by aminolysis reaction with excess of DET molecules. The ^{1}H NMR measurement revealed the quantitative introduction of the *N*-(2-aminoethyl)-2-aminoethyl moiety for successful synthesis of PEG-PAsp(DET) (data not shown). Further, the *cis*-aconityl moiety (Aco) was introduced into the primary amine in the side chain of PAsp(DET) by reacting *cis*-aconitic anhydride with PEG-PAsp(DET) to form an acid-labile *cis*-aconitylamide in the side chain. The quantitative conversion of primary

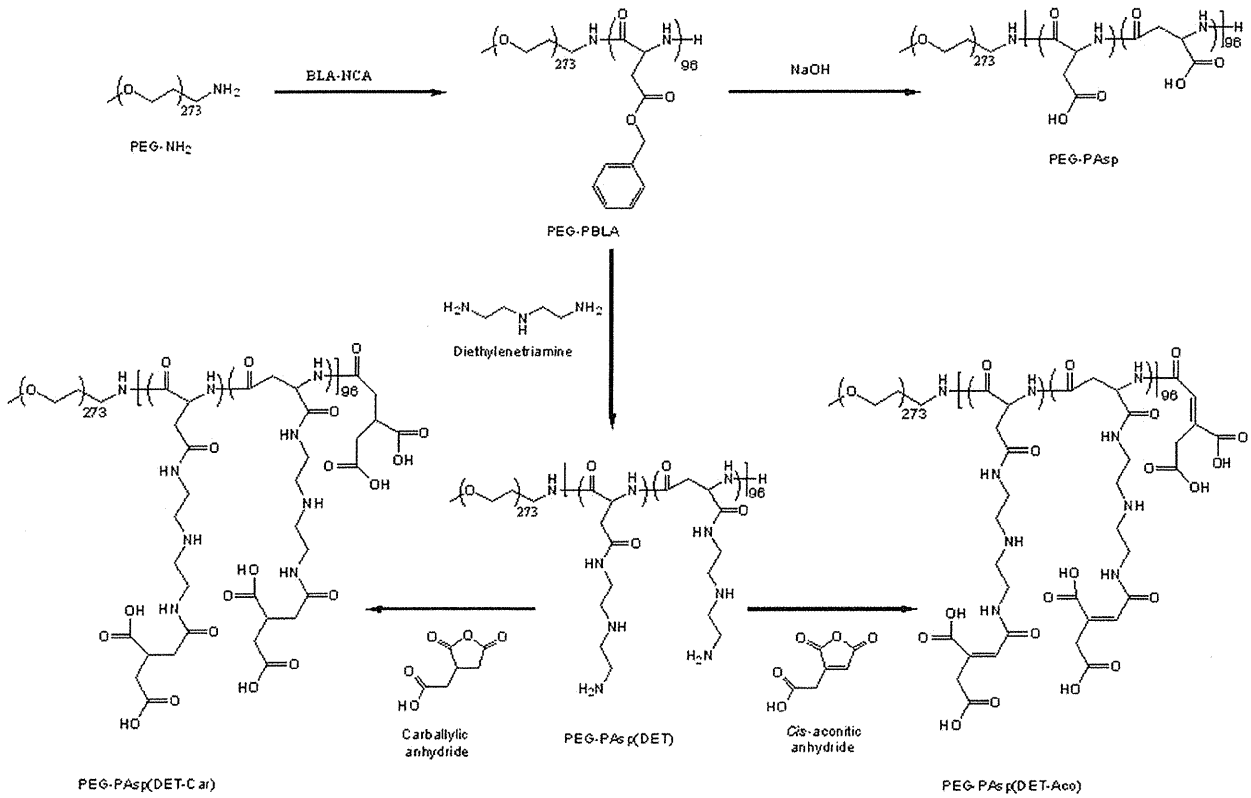

Scheme 1. Synthetic routes of PEG-PAsp(DET-Aco), PEG-PAsp(DET-Car), and PEG-PAsp.

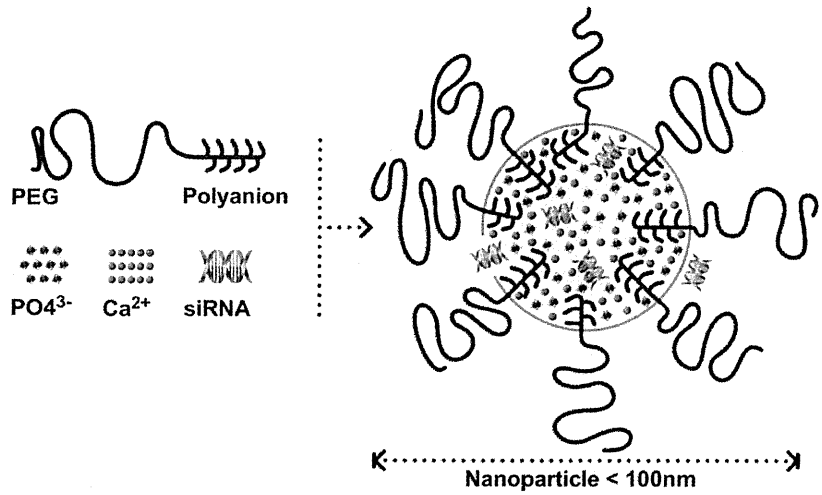

Fig. 2. Schematic illustration of PEG-polyanion/siRNA/CaP hybrid nanoparticles.

amines in Asp(DET) side chain to *cis*-aconitylamide was confirmed from the peak intensity ratio of the methine protons in the main chain to methine protons of the *cis*-aconityl moiety in the ^{1}H NMR spectrum in D_2O (Fig. 1). Although it was also possible to observe the formation of reaction subproducts [27], the desired product of PEG-PAsp(DET-Aco) was obtained in a high ratio (80%). PEG-PAsp (DET-Car) without the acid-labile bond as a control was synthesized by reacting PEG-PAsp(DET) with carballylic anhydride similarly. The quantitative conversion of the primary amines in the Asp(DET) side chain to carballylylamide was confirmed from the peak intensity ratio of the methine protons in the main chain to the methine and methylene protons of carballylyl moiety in the ^{1}H NMR spectrum in D_2O (Supporting Information). In addition, another control polyanion, PEG-PAsp, was prepared by the deprotection of benzyl ester group from PEG–PBLA. The successful deprotection of benzyl ester group was confirmed from the corresponding peak disappearance in the ^{1}H NMR spectrum in D_2O (data not shown). Note that all the reactions were confirmed to proceed without the spontaneous main-chain cleavage [21] from aqueous GPC charts of obtained polymers (data not shown).

3.2. PEG-polyanion/siRNA/CaP hybrid nanoparticle formation and characterization

Great advantages in the utilization of CaP precipitates as a transfection reagent are the fact that they are prepared by a simple and inexpensive method, and also that it efficiently binds/encapsulates polyanions/nucleic acids during the formation process [28,29]. Through self-assembly, CaP nanoparticles containing nucleic acid are formed by the precipitation method in which calcium chloride and phosphate solutions are mixed in the presence of siRNA. However, simple CaP precipitates have potential problems to overcome for efficient nucleic acids delivery; one is the increase in size with time to form large agglomerates in aqueous solutions, and another is poor endosomal escape. To prevent the size increase in CaP precipitates, our previous studies have addressed a preparation of PEG-coated CaP hybrid nanoparticles by mixing of PEG-polyanion block copolymers [9,11–14]. In this study, for further improvement of the PEG-coated CaP nanoparticles, we focused on endosomal escape of the nanoparticles to enhance the gene knockdown efficiency, thus applying a charge-conversional structure PAsp(DET-Aco) [23,24] for the polyanionic segment. Indeed, the hybrid nanoparticles were prepared from the inorganic CaP core, siRNA as a therapeutic payload, and the PEG-PAsp(DET-Aco) as a charge-conversional unit for endosomal escape with minimal cytotoxicity, by mixing calcium and phosphate ionic solutions containing siRNA and the charge-conversional polymer as illustrated in Fig. 2.

The TEM observations with uranyl acetate as a staining agent (Fig. 3A) revealed hybrid nanoparticles with relatively homogenous spherical shape and average size of 42 ± 5 nm. Furthermore, the DLS measurements provided a size histogram in number statistics showing a narrow unimodal distribution with the peak at 38 nm

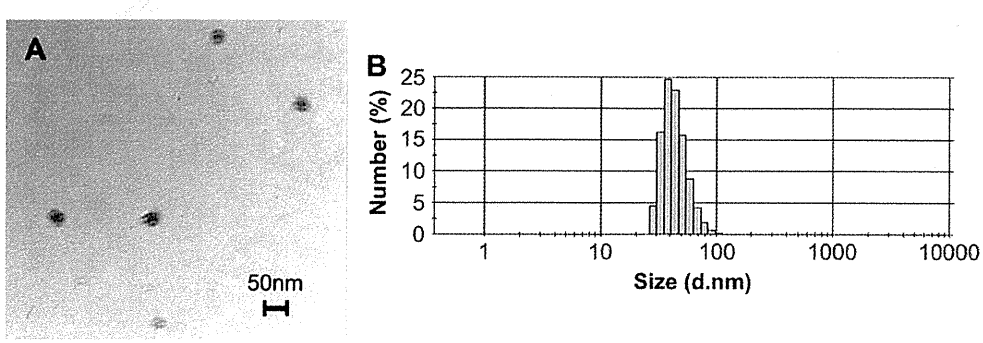

Fig. 3. Size and morphology of PEG-PAsp(DET-Aco)/siRNA/CaP hybrid nanoparticles. A: TEM image (Scale Bar: 50 nm). B: Histogram in number statistics determined by DLS measurement (1 mg/mL PEG-PAsp(DET-Aco) and 3 μM siRNA).

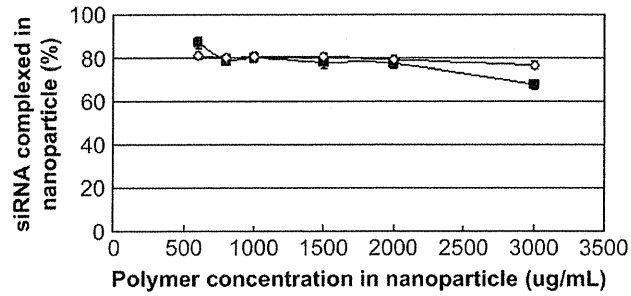

Fig. 4. Percentage of siRNA loaded by the hybrid nanoparticle at varying polymer concentrations (3 μM siRNA). Closed square: PEG-PAsp(DET-Aco), Open diamond: PEG-PAsp(DET-Car).

(Fig. 3B), which was well correlated to the size determined by the TEM observations (Fig. 3A). Samples were confirmed to have the same size even after prolonged incubation time. These results indicate that hybrid nanoparticles can be obtained in a controllable manner using the charge-conversional polymer as colloidal stability agent.

The amount of siRNA encapsulated in the hybrid nanoparticles was monitored against polyanion concentration, determined by the centrifugal assay as previously reported [11]. Effective encapsulation of siRNA in the nanoparticles (around 80%) was confirmed in PEG-PAsp(DET-Aco) concentration between 600 and 2000 μg/mL, while a slight decrease was observed at the concentration of 3000 μg/mL (around 70%) (Fig. 4). Note that the similar binding tendency was observed for the nanoparticle from PEG-PAsp(DET-Car). The siRNA-loading capacities obtained here were close to those found in our previous work with PEG-PAsp (around 85%) [11], indicating efficient entrapment of siRNA by this method regardless of polyanion structures.

3.3. Gene knockdown and cell viability assays

The development of an effective and non-cytotoxic carrier is the main challenge to the success in RNAi therapy. We verified the gene knockdown efficiency of the hybrid nanoparticles to a cultured pancreatic cancer cell (PanC-1) by measuring the level of mRNA. Here, vascular endothelial growth factor (VEGF) was chosen as a target gene because many cancer cells up-regulate VEGF expression to promote angiogenesis, a process characterized by the formation of new blood vessels from a pre-existing vascular network [30,31], facilitating the tumor growth and proliferation. Hence, VEGF knockdown in such cancer cells with siRNA *in vivo* is expected to be a promising strategy to suppress the tumor growth and control cancer evolution (anti-angiogenic therapy).

Hybrid nanoparticles containing 60 nM siVEGF or siLuc as a non-targeted control sequence were applied to PanC-1 cells, and after 3 h of exposure time the medium was replaced and cells were further incubated for 24 h. Thereafter, the real-time RT-PCR analysis was used to determine the mRNA for VEGF. The results revealed that all the tested hybrid nanoparticles with siVEGF possessed potential gene knockdown activity, whereas the nanoparticles with siLuc and naked siVEGF showed no gene knockdown (Fig. 5), indicating the siVEGF sequence-specific gene knockdown with the hybrid nanoparticles. Among them, the nanoparticle from PEG-PAsp(DET-Aco) presented the only significant and highest gene knockdown (~82%). The comparison of PEG-PAsp(DET-Aco) with the other PEG-polyanions strongly suggests that the acid-labile *cis*-aconitylamide in PEG-PAsp(DET-Aco) should be essential for the significant gene knockdown. Next, the cytotoxicity of the hybrid nanoparticles was evaluated to PanC-1 cells. A wide range of siRNA concentration was tested from 10 to 1500 nM along with the increase in all the other components. As shown in Fig. 6, no significant cytotoxicity was observed for both hybrid nanoparticles from PEG-PAsp(DET-Aco/Car) even at the highest concentration (50 μg/mL PEG-polyanion, 1.5 μM siRNA). From these results, we concluded that the hybrid nanoparticles from PEG-PAsp(DET-Aco) allowed efficient siRNA delivery into the cytoplasm of cultured PanC-1 with negligible cytotoxicity.

3.4. Cellular uptake and intracellular trafficking

In siRNA transfection process, after cellular internalization as the first hurdle, siRNA carriers will be delivered to early endosomes,

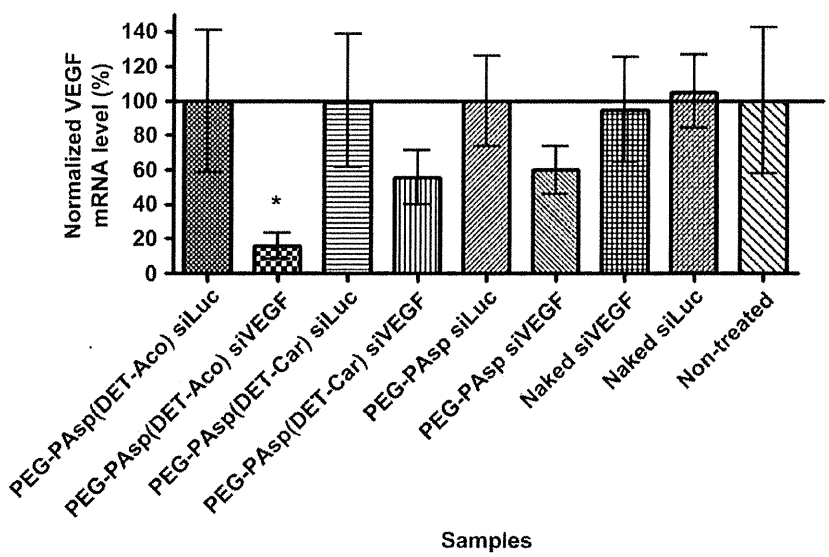

Fig. 5. Gene knockdown in PanC-1 at 24 h after 3 h of nanoparticles exposition to cells (60 nM siRNA, $N = 9$). Controls were set as 100%. *$p < 0.05$ comparing to controls (ANOVA followed by Bonferroni).

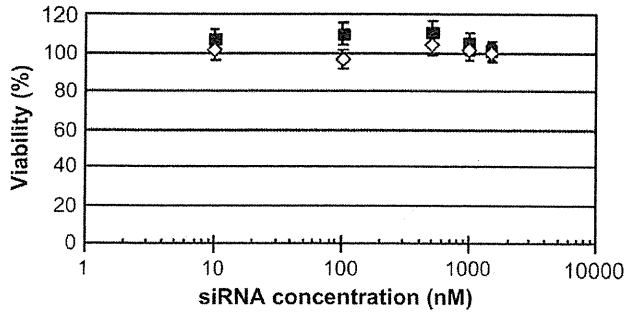

Fig. 6. Cell viability of PanC-1 cells incubated with hybrid nanoparticles for 48 h ($N = 6$). siLuc concentration was changed from 10 to 1500 nM, corresponding to the polymer concentration from 0.7 to 50 μg/mL. Closed square: PEG-PAsp(DET-Aco), Open diamond: PEG-PAsp(DET-Car).

followed by the movement to late endosomes/lysosomes for siRNA degradation [6]. Thus, the smooth endosomal escape is a critical requirement for the effective gene silencing with siRNA. In the preceding section, the utility of PEG-PAsp(DET-Aco) was demonstrated for significant VEGF mRNA knockdown without marked cytotoxicity. Here, we verified whether the excellent gene knockdown is attributed to endosomal escape with PEG-PAsp(DET-Aco) along with our initial hypothesis. Accordingly, we observed the intracellular trafficking of each hybrid nanoparticle after 3- and 24-h incubation with PanC-1 cells. In the obtained images, Cy5-siRNA, endosomes/lysosomes, and nuclei were shown in red, green, and blue, respectively, and thus yellow pixels result in the merge of red and green pixels, indicating the co-localization of Cy5-siRNA with endosome/lysosome. The images of PanC-1 cells treated with PEG-PAsp(DET-Aco)/PEG-PAsp(DET-Car) nanoparticles displayed red and/or yellow regions with 3-h incubation (Fig. 7A and B), indicating that both of the nanoparticles allowed the significant cellular uptake of Cy5-siRNA. In these two images, only the nanoparticles containing PEG-PAsp(DET-Aco) in the formulation presented widely extended red regions in cells (Fig. 7A), corresponding to the presence of Cy5-siRNA in the cytoplasm. In contrast, the cells treated with the other nanoparticles containing PEG-PAsp(DET-Car) mainly displayed perinuclear yellow spots (Fig. 7B), indicating the endosomal/lysosomal capture of Cy5-siRNA. These results are well consistent with our hypothesis that the integration of PEG-PAsp(DET-Aco) into the nanoparticles intensely facilitates the endosomal escape of the hybrid nanoparticles in the early stage of transfection, presumably due to the charge-conversional property

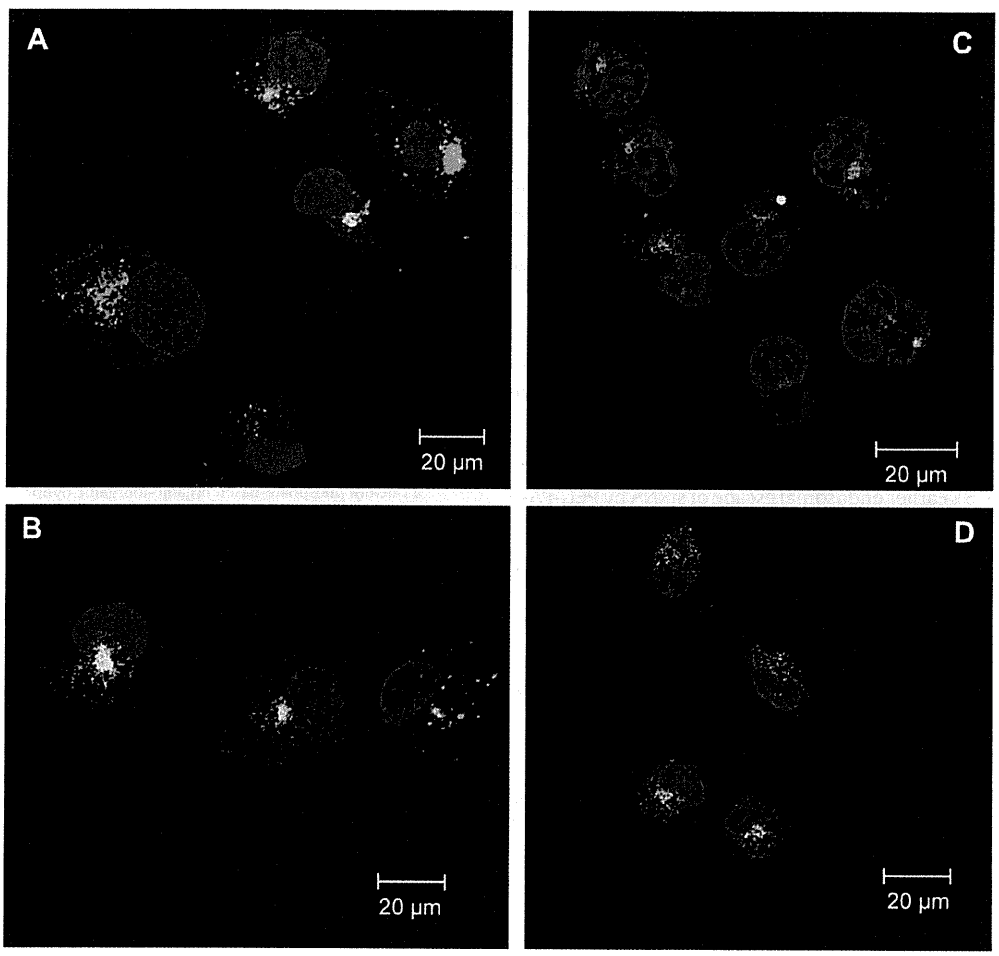

Fig. 7. Confocal laser scanning microscopic observation for intracellular trafficking of hybrid nanoparticles. Images were taken at 3 and 24 h after nanoparticle application. A: PEG-PAsp(DET-Aco), B: PEG-PAsp(DET-Car) nanoparticles incubated for 3 h (100 nM siRNA). C: PEG-PAsp(DET-Aco), D: PEG-PAsp(DET-Car) nanoparticles incubated for 24 h (100 nM siRNA). Blue: Hoechst at 710 nm (two-photon excitation); Green: Lysotracker at 488 nm; and Red: Cy5 at 633 nm.

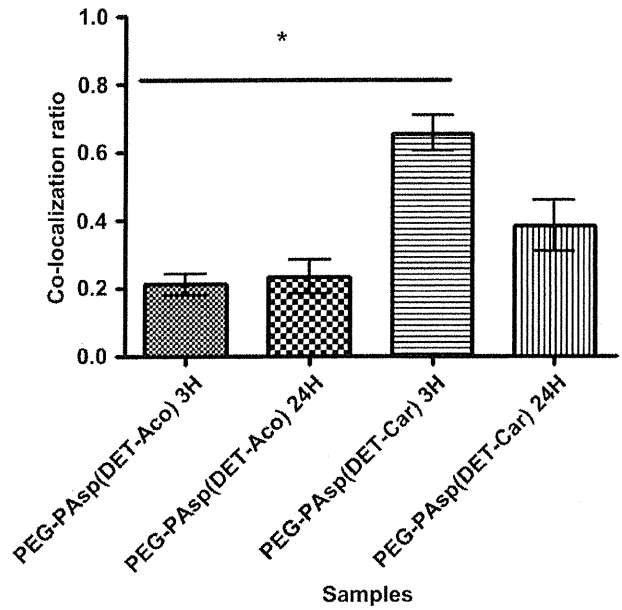

Fig. 8. Co-localization ratio of Cy5-labeled siRNA with endosome/lysosome obtained by analyzing the images. Results were expressed as mean ± SEM (from three cells) (*$p < 0.01$).

to reproduce the endosomal membrane destabilizing polycation, PAsp(DET), in the acidic endocytic vesicles. On the other hand, after 24-h incubation, the cells treated with PEG-PAsp(DET-Car) nanoparticles obviously increased red regions (Fig. 7D), suggesting that the hybrid nanoparticles might originally have an endosomal escaping ability apart from the charge-conversional polymers. A possible explanation of this delayed endosomal escape is that CaP core disassembles under a low ionic condition in endocytic vesicles for increased-ion induced-osmotic pressure to induce endosomal membrane disruption [11], similar to the proton sponge hypothesis known to polyethyleneimine [32]. Eventually, the co-localization of Cy5-siRNA with endosome/lysosome was quantitatively analyzed for PEG-PAsp(DET-Aco) and PEG-PAsp(DET-Car), as summarized in Fig. 8. The obtained tendency in endosomal escape of each nanoparticle is well correlated with the result in the gene knockdown experiment (Fig. 5). Earlier endosomal escape of siRNA by PEG-PAsp (DET-Aco) probably leads to more efficient gene knockdown with the nanoparticles.

4. Conclusion

This work was aimed to develop a hybrid nanocarrier system consisting of CaP and the PEG–charge-conversional polymer for safe and efficient siRNA delivery. To improve the endosomal escape of the nanoparticles, we integrated the charge-conversional polymer PEG-PAsp(DET-Aco) into the nanoparticles, in which PEG-PAsp (DET-Aco) induces the destabilization of endosomal membrane by producing a polycation PAsp(DET) via the selective cleavage of *cis*-aconitylamide in acidic endosome/lysosome. The size less than 100 nm with narrow size distribution and a high siRNA-loading capacity were confirmed for PEG-PAsp(DET-Aco)/siRNA/CaP nanoparticles, which achieved strong VEGF knockdown to PanC-1 with negligible cytotoxicity through the rapid endosomal escape. These findings demonstrate our hybrid system as a promising candidate to future *in vivo* siRNA applications for pancreatic cancer treatment based on anti-angiogenic therapy.

Acknowledgments

This research is supported by the Japan Society for the Promotion of Science (JSPS) through its "Funding Program for World-Leading Innovative R&D on Science and Technology (FIRST Program)". F.P. acknowledges the fellowship from Ministry of Education, Science, Sports and Culture, Japan (MEXT).

Appendix

Figures with essential color discrimination. Figs. 2, 3 and 7 in this article are difficult to interpret in black and white. The full color images can be found in the online version, at doi:10.1016/j.biomaterials.2010.12.057.

Appendix. Supporting information

Supplementary data associated with this article can be found, in the online version, at doi:10.1016/j.biomaterials.2010.12.057.

References

[1] Fire A, Xu S, Montgomery MK, Kostas SA, Driver SE, Mello CC. Potent and specific genetic interference by double-stranded RNA in *Caenorhabditis elegans*. Nature 1998;391:806–11.
[2] Elbashir SM, Harborth J, Lendeckel W, Yalcin A, Weber K, Tuschl T. Duplexes of 21-nucleotide RNAs mediate RNA interference in cultured mammalian cells. Nature 2001;411:494–8.
[3] International Human Genome Sequencing Consortium. Initial sequencing and analysis of the human genome. Nature 2001;409:860–921.
[4] Venter JC, Adams MD, Myers EW, Li PW, Mural RJ, Sutton GG, et al. The sequence of the human genome. Science 2001;291:1304–51.
[5] International Human Genome Sequencing Consortium. Finishing the euchromatic sequence of the human genome. Nature 2004;431:931–45.
[6] Whitehead KA, Langer R, Anderson DG. Knocking down barriers: advances in siRNA delivery. Nat Rev Drug Discov 2009;8(2):129–38.
[7] Graham FL, van der Eb AJ. A new technique for the assay of infectivity of human adenovirus 5 DNA. Virology 1973;52:456–67.
[8] Jordan M, Schallhorn A, Wurm FM. Transfecting mammalian cells: optimization of critical parameters affecting calcium–phosphate precipitate formation. Nucleic Acids Res 1996;24:596–601.
[9] Kakizawa Y, Kataoka K. Block copolymer self-assembly into monodispersive nanoparticles with hybrid core of antisense DNA and calcium phosphate. Langmuir 2002;18:4539–43.
[10] Maitra A. Calcium phosphate nanoparticles: second-generation nonviral vectors in gene therapy. Expert Rev Mol Diagn 2005;5(6):893–905.
[11] Kakizawa Y, Furukawa S, Kataoka K. Block copolymer-coated calcium phosphate nanoparticles sensing intracellular environment for oligodeoxynucleotide and siRNA delivery. J Control Release 2004;97:345–56.
[12] Kakizawa Y, Miyata K, Furukawa S, Kataoka K. Size-controlled formation of a calcium phosphate-based organic-inorganic hybrid vector for gene delivery using poly(ethylene glycol)-*block*-poly(aspartic acid). Adv Mater 2004;16 (8):699–702.
[13] Kakizawa Y, Furukawa S, Ishii A, Kataoka K. Organic–inorganic hybrid-nanocarrier of siRNA constructing through the self-assembly of calcium phosphate and PEG-based block aniomer. J Control Release 2006;111:368–70.
[14] Zhang MZ, Ishii A, Nishiyama N, Matsumoto S, Ishii T, Yamasaki Y, et al. PEGylated calcium phosphate nanocomposites as smart environment-sensitive carriers for siRNA delivery. Adv Mater 2009;21(34):3520–5.
[15] Francis G, Delgado C, Fisher D, Malik F, Agrawal AK. Polyethylene glycol modification: relevance to improved methodology to tumour targeting. J Drug Target 1996;3:321–40.
[16] Monfardini C, Veronese FM. Stabilization of substances in the circulation. Bioconjug Chem 1998;9:418–50.
[17] Kataoka K, Harada A, Nagasaki Y. Block copolymer micelles for drug delivery: design, characterization and biological significance. Adv Drug Deliv Rev 2001;47:113–31.
[18] Dominska M, Dykxhoorn DM. Breaking down the barriers: siRNA delivery and endosome escape. J Cell Sci 2010;123:1183–9.
[19] Kanayama N, Fukushima S, Nishiyama N, Itaka K, Jang W-D, Miyata K, et al. A PEG-based biocompatible block catiomer with high buffering capacity for the construction of polyplex micelles showing efficient gene transfer toward primary cells. ChemMedChem 2006;1:439–44.
[20] Miyata K, Oba M, Nakanishi M, Fukushima S, Yamasaki Y, Koyama H, et al. Polyplexes from poly(aspartamide) bearing 1,2-diaminoethane side chains induce pH-selective, endosomal membrane destabilization with amplified transfection and negligible cytotoxicity. J Am Chem Soc 2008;130(48): 16287–94.

[21] Itaka K, Ishii T, Hasegawa Y, Kataoka K. Biodegradable polyamino acid-based polycations as safe and effective gene carrier minimizing cumulative toxicity. Biomaterials 2010;31(13):3707–14.
[22] Kim HJ, Ishii A, Miyata K, Lee Y, Wu S, Oba M, et al. Introduction of stearoyl moieties into a biocompatible cationic polyaspartamide derivative, PAsp (DET), with endosomal escaping function for enhanced siRNA-mediated gene knockdown. J Control Release 2010;145(2):141–8.
[23] Lee Y, Miyata K, Oba M, Ishii T, Fukushima S, Han M, et al. Charge conversion ternary polyplex with endosomes disruption moiety: a technique for efficient and safe gene delivery. Angew Chem Int Ed Engl 2008;120:5241–4.
[24] Sanjoh M, Hiki S, Lee Y, Oba M, Miyata K, Ishii T, et al. pDNA/poly(l-lysine) polyplexes functionalized with a pH-sensitive charge-conversional poly (aspartamide) derivative for controlled gene delivery to human umbilical vein endothelial cells. Macromol Rapid Commun 2010;31(13):1181–6.
[25] Lee Y, Fukushima S, Bae Y, Hiki S, Ishii T, Kataoka K. A protein nanocarrier from charge-conversion polymer in response to endosomal pH. J Am Chem Soc 2007;129:5362–3.
[26] Elgazwy A-SSH. Facile synthesis of (*R*, *R*) and of (*R*, *S*) tricarballylic acid anhydride and imide derivatives. Molecules 2000;5:665–73.
[27] Dinand E, Zloh M, Brocchini S. Competitive reactions during amine addition to *cis*-aconityl anhydride. Aust J Chem 2002;55:467–74.
[28] Sokolova VV, Radtke I, Heumann R, Epple M. Effective transfection of cells with multi-shell calcium phosphate–DNA nanoparticles. Biomaterials 2006;27:3147–53.
[29] Zhang M, Kataoka K. Nano-structured composites based on calcium phosphate for cellular delivery of therapeutic and diagnostic agents. Nano Today 2009;4:508–17.
[30] Sullivan LA, Brekken RA. The VEGF family in cancer and antibody-based strategies for their inhibition. MAbs 2010;2(2):165–75.
[31] Dvorak HF. Vascular permeability factor/vascular endothelial growth factor: a critical cytokine in tumor angiogenesis and a potential target for diagnosis and therapy. J Clin Oncol 2002;20:4368–80.
[32] Boussif O, Lezoualc'h F, Zanta MA, Mergny MD, Scherman D, Demeneix B, et al. A versatile vector for gene and oligonucleotide transfer into cells in culture and *in vivo*: polyethylenimine. Proc Natl Acad Sci U S A 1995;92:7297–301.

DRUG DELIVERY

Improving Drug Potency and Efficacy by Nanocarrier-Mediated Subcellular Targeting

Mami Murakami,[1] Horacio Cabral,[1,2] Yu Matsumoto,[3] Shourong Wu,[3] Mitsunobu R. Kano,[4] Takao Yamori,[5] Nobuhiro Nishiyama,[2,3]* Kazunori Kataoka[1,2,3,6]*

Nanocarrier-mediated drug targeting is an emerging strategy for cancer therapy and is being used, for example, with chemotherapeutic agents for ovarian cancer. Nanocarriers are selectively accumulated in tumors as a result of their enhanced permeability and retention of macromolecules, thereby enhancing the antitumor activity of the nanocarrier-associated drugs. We investigated the real-time subcellular fate of polymeric micelles incorporating (1,2-diaminocyclohexane) platinum(II) (DACHPt/m), the parent complex of oxaliplatin, in tumor tissues by fluorescence-based assessment of their kinetic stability. These observations revealed that DACHPt/m was extravasated from blood vessels to the tumor tissue and dissociated inside each cell. Furthermore, DACHPt/m selectively dissociated within late endosomes, enhancing drug delivery to the nearby nucleus relative to free oxaliplatin, likely by circumvention of the cytoplasmic detoxification systems such as metallothionein and methionine synthase. Thus, these drug-loaded micelles exhibited higher antitumor activity than did oxaliplatin alone, even against oxaliplatin-resistant tumors. These findings suggest that nanocarriers targeting subcellular compartments may have considerable benefits in clinical applications.

INTRODUCTION

In 2009, about 10 million people worldwide were newly diagnosed with cancer (*1*). Application of nanotechnology to cancer therapy may offer therapeutic effects that cannot be achieved with other strategies. The main aim of this approach is to develop nanoscale drug vehicles for targeted cancer therapy (*2–5*). Nanocarriers selectively accumulate in solid tumors as a result of the enhanced permeability and retention (EPR) effect, which is characterized by microvascular hyperpermeability to circulating macromolecules and impaired lymphatic drainage in tumor tissues (*6*). At present, several nanocarrier formulations have been approved for clinical use against ovarian cancer and HIV-associated Kaposi's sarcoma (Doxil) and breast cancer (Abraxane). These formulations allow better accumulation of the drugs doxorubicin and paclitaxel in tumors (*7*).

Polymeric micelles, self-assemblies of block copolymers, have gained increasing popularity as tumor-targetable nanocarriers since they were first used as drug vehicles in the late 1980s (*8–12*). These micelles, which are several tens of nanometers in size and have a characteristic core-shell structure consisting of a drug-loaded hydrophobic core and poly(ethylene glycol) (PEG) hydrophilic shell, are long-lived in the bloodstream and effectively accumulate in solid tumors after intravenous injection (*8*). The critical features of polymeric micelles for their function as drug vehicles, including size, drug loading and release, and specific binding to the target cells, can be modulated by engineering the constituent block copolymers. At present, our micelle formulations incorporating doxorubicin, paclitaxel, SN-38, cisplatin, and (1,2-diaminocyclohexane) platinum(II) (DACHPt) are undergoing clinical trials (development code names NK911, NK105, NK012, NC-6004, and NC-4016, respectively), and four of these have advanced to Phase II studies (*13–17*). These clinical studies have revealed that polymeric micelles reduce side effects from the incorporated drugs and are effective against various intractable tumors, such as triple-negative breast cancers (*18*), indicating their clinical potential.

Recently, increasing attention has been paid to another potentially useful property of nanocarriers: to achieve subcellular drug targeting. Subcellular drug targeting of nanocarriers could enhance the pharmacological activity of the loaded drugs through improved subcellular drug distribution (*19*). Drug vehicles designed to release active drugs in acidic organelles, such as the endosome and lysosome, can circumvent recognition by the drug efflux pump (for example, P-glycoprotein) through internalization by endocytosis, thus overcoming multidrug resistance in cancer cells (*20–22*). Here, we aimed to investigate the potential of DACHPt-loaded micelles (DACHPt/m) for in vivo subcellular targeting. DACHPt/m is formed by the polymer-metal complexation between DACHPt and the carboxylic group of poly(ethylene glycol)-*b*-poly(glutamic acid) [PEG-*b*-P(Glu)] copolymers. DACHPt is the parent complex of the clinically approved drug oxaliplatin. Oxaliplatin has a hydrolyzable oxalate group to increase its solubility in water, which can be removed by nucleophiles in biological media, such as chloride ions. Aqua complexes ($[(DACH)Pt(H_2O)Cl]^+$ or $[(DACH)Pt(H_2O)_2]^{2+}$) of DACHPt exhibit chemotherapeutic activity. DACHPt/m releases DACHPt and the micelle structure dissociates depending on the pH and chloride ion concentrations, a result of ligand substitution of the Pt(II) from the carboxylates in the micelle core with the chloride ions in the medium (Fig. 1A) (*23, 24*). Moreover, after DACHPt/m is internalized into cancer cells, it would be expected to be exposed to different pH and chloride ion concentrations during subcellular trafficking (*25*). We hypothesized that DACHPt/m would be selectively released in low-pH cellular compartments, bypassing

[1]Department of Bioengineering, Graduate School of Engineering, University of Tokyo, 7-3-1 Hongo, Bunkyo-ku, Tokyo 113-8656, Japan. [2]Center for NanoBio Integration, University of Tokyo, Tokyo 113-8656, Japan. [3]Center for Disease Biology and Integrative Medicine, Graduate School of Medicine, University of Tokyo, Tokyo 113-0033, Japan. [4]Department of Molecular Pathology, Graduate School of Medicine, University of Tokyo, Tokyo 113-0033, Japan. [5]Division of Molecular Pharmacology, Cancer Chemotherapy Center, Japanese Foundation for Cancer Research, 3-10-6 Ariake, Koto-ku, Tokyo 135-8550, Japan. [6]Department of Materials Engineering, Graduate School of Engineering, University of Tokyo, Tokyo 113-8656, Japan.
*To whom correspondence should be addressed. E-mail: nishiyama@bmw.t.u-tokyo.ac.jp (N.N.); kataoka@bmw.t.u-tokyo.ac.jp (K.K.)

cytoplasmic detoxification and thereby improving potency and efficacy (Fig. 1B). Indeed, we previously reported that cisplatin-loaded micelles, which are formed in the same manner as DACHPt/m, caused different gene expression patterns than did cisplatin alone because of their different internalization pathways and the facilitated drug release in endosomes and lysosomes (*26*). To test the above-mentioned hypothesis, we constructed fluorescent-labeled DACHPt/m (F-DACHPt/m) with a dual fluorescent-labeling method so that we could follow the intracellular localization and dissociation of the micelles by using in vivo confocal microscopy, and intravitally evaluated the extravasation, penetration, cellular uptake, and subcellular fate of DACHPt/m in tumor tissues and their activity against human colorectal cancers.

RESULTS

Construction and characterization of F-DACHPt/m

To construct the dual fluorescent-labeled block copolymer, we conjugated the fluorescent dyes boron dipyrromethene (BODIPY) FL (excitation wavelength, 503 nm; emission wavelength, 512 nm) and BODIPY TR (excitation wavelength, 588 nm; emission wavelength, 616 nm) to the α- and ω-end groups of α-4-(diethoxymethyl)benzyl-poly(ethylene glycol)-*b*-poly(L-glutamic acid), respectively, and thus obtained BODIPY FL-PEG-*b*-P(Glu)-BODIPY TR (fig. S1). The conjugation degree for BODIPY FL to the block copolymer was 0.2 mol BODIPY FL per mole of polymer and for BODIPY TR was about 0.8 mol BODIPY TR per mole of polymer. We built F-DACHPt/m by the formation of polymer-metal complexes between DACHPt and the carboxylic groups of poly(glutamic acid) in BODIPY FL-PEG-*b*-P(Glu)-BODIPY TR (Fig. 1A). F-DACHPt/m had a diameter of 30 nm, similar to that of DACHPt/m (fig. S2). The intact F-DACHPt/m emitted fluorescence only from the shell-conjugated dye (BODIPY FL) because the core-conjugated dye (BODIPY TR) was quenched owing to its high local concentration. The close proximity of BODIPY TR fluorophores in the core of the micelles leads to self-quenching by the formation of nonfluorescent ground-state BODIPY TR dimers (or higher aggregates) (*27*). When DACHPt is released as a result of the ligand substitution of the Pt(II) from the carboxylates in the micelle core with the chloride in the medium, the density of the micelle core is reduced and the fluorescence of BODIPY TR is dequenched (Fig. 1A). We investigated the release of DACHPt from F-DACHPt/m and the fluorescence of BODIPY FL and BODIPY TR at the surface and core of the micelles, respectively, under conditions that mimicked the extracellular medium (pH 7.4 and 150 mM Cl^-), early endosomes (pH 6.9 and 20 mM Cl^-), and late endosomes and lysosomes (pH 5.5 and 70 mM Cl^-) (*25*). The fluorescence from BODIPY FL on the shell of the micelles was constant regardless of the pH and salt concentration of the media (Fig. 2, A to C, middle columns), suggesting that the fluorescence from BODIPY FL can be used to trace the position of the micelles in the biological environment. In addition, the drug release profile of F-DACHPt/m was similar to that of unmodified DACHPt/m, suggesting the feasibility of a direct comparison (Fig. 2, A to C, left columns). Under extracellular conditions, BODIPY TR fluorescence increased after an incubation period of 17 hours, simultaneous with the release of DACHPt from F-DACHPt/m (Fig. 2A). The release of DACHPt from F-DACHPt/m in the late endosomal conditions was considerably faster (Fig. 2C) than in the extra-

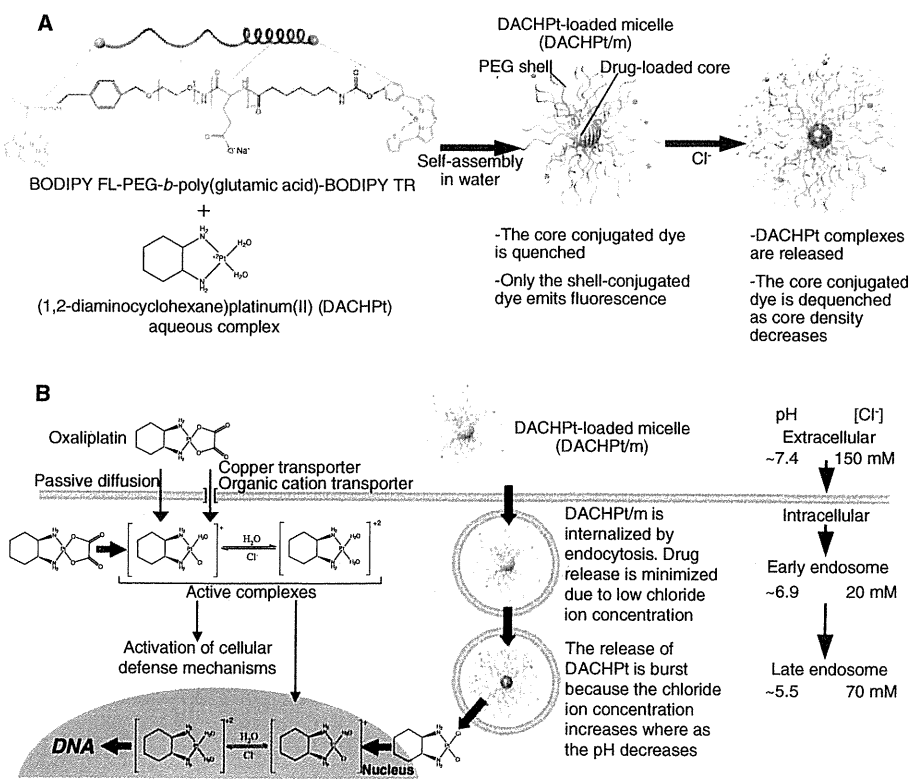

Fig. 1. Design of fluorescent-labeled DACHPt/m (F-DACHPt/m) for visualization of the localization and drug release in the cell. (**A**) F-DACHPt/m self-assembled through polymer-metal complex formation between DACHPt and boron dipyrromethene (BODIPY) FL–poly(ethylene glycol)-*b*-poly(glutamic acid)–BODIPY TR in distilled water. In the micelle state, only BODIPY FL (green) emits fluorescence, whereas BODIPY TR (red) remains quenched. As DACHPt is released from F-DACHPt/m in chloride ion–containing media, BODIPY TR is dequenched and emits fluorescence. (**B**) Schematic representation of hypothetical subcellular pathways and action of DACHPt/m. Oxaliplatin enter cells by passive diffusion or through copper/organic cation transporters. Once oxaliplatin is in the cytoplasm, most of the activated aqua species ($[(DACH)Pt(H_2O)Cl]^+$ or $[(DACH)Pt(H_2O)_2]^{2+}$) are eliminated by cellular detoxification mechanisms, but a small fraction binds to DNA. In contrast, DACHPt/m that enters tumor cells by endocytosis (middle) is exposed to an environment with increasing acidity and chloride ion concentration because early endosomes mature into the late endosomes. Drug release from DACHPt/m is accelerated in the late endosomal environment close to the perinuclear region, resulting in enhanced efficiency of drug delivery to the nucleus.

cellular and early endosomal conditions (Fig. 2, A and B), occurring without any delay. Further, mirroring the DACHPt release, F-DACHPt/m exhibited more robust fluorescence recovery of BODIPY TR under the late endosomal conditions (Fig. 2C) than under the early endosomal conditions (Fig. 2B, right columns). Thus, the fluorescence profiles of BODIPY TR are correlated with the release profiles of DACHPt from the micelles.

In vitro subcellular trafficking of F-DACHPt/m

The cellular internalization and fate of F-DACHPt/m in human tumor-derived colorectal cancer (HT29) cells, which are the most frequently used cell lines in oxaliplatin studies (*28*), were observed with time-lapse confocal laser scanning microscopy (CLSM) (Fig. 3A and video S1). The intensity of BODIPY FL fluorescence increased slightly over time (Fig. 3B), and the BODIPY FL fluorescence in the images was clearly visible within a 6-hour incubation (Fig. 3A). Meanwhile, with time, the intensity of BODIPY TR fluorescence continuously increased to a greater extent than did that of BODIPY FL fluorescence (Fig. 3B), and the BODIPY TR fluorescence in the images became visible at about 24 hours of incubation (Fig. 3A). This continuous increase in the intensity of BODIPY TR fluorescence corresponds to the dequenching of BODIPY TR fluorescence driven by the release of DACHPt in the cell. These results suggest that F-DACHPt/m enters the cells as a micelle form and then dissociates within the subcellular environments.

Using CLSM with higher magnification, we further evaluated the detailed subcellular trafficking and fate of F-DACHPt/m by focusing on individual cells. We confirmed that the micelles entered the cancer cells via endocytosis by incubating the cells with F-DACHPt/m at 37°C and 4°C. As endocytosis ceases at 4°C, the fluorescent signal of F-DACHPt/m inside the cells was undetectable, whereas at 37°C, the fluorescence from F-DACHPt/m was observed inside the cells (fig. S3). To examine the subcellular trafficking of the micelles, we determined the colocalization of BODIPY FL fluorescence from F-DACHPt/m with an early endosome marker, Rab5a-RFP, and a late endosome and lysosome marker, LysoTracker, in HT29 cells (Fig. 3C). Note that individual vesicular organelles can be recognized as punctate fluorescence in the images. After a 6-hour incubation at 37°C, BODIPY FL colocalized mainly with Rab5a-RFP (yellow fluorescence in Fig. 3C, upper images) rather than with LysoTracker. After prolonged incubation (24 and 55 hours), BODIPY FL showed decreased colocalization with Rab5a-RFP and increased colocalization with LysoTracker (yellow fluorescence in Fig. 3C, lower images). This observation was confirmed by quantification of colocalized fluorescent intensities of BODIPY FL with Rab5a-RFP or LysoTracker (Fig. 3D). These results suggested that the micelles might localize mainly in the early endosome until 6 hours and then move into the late endosome/lysosome compartment. Furthermore, we studied the timing and location of the micelle dissociation and concomitant drug release by evaluating the colocalization of F-DACHPt/m with LysoTracker (Fig. 3E and fig. S4A) and the quantification of BODIPY FL and BODIPY TR fluorescent intensities (fig. S4B), as well as the colocalization ratio (Fig. 3F). The fluorescence intensity from BODIPY FL gradually increased (fig. S4B). Meanwhile, the fluorescence of BODIPY TR became visible after 24-hour incubation (Fig. 3E and fig. S4A) and then increased over time (fig. S4B). Both BODIPY FL and BODIPY TR colocalized with LysoTracker (Fig. 3E and fig. S4A), and the colocalization ratio between BODIPY FL or BODIPY TR and LysoTracker increased over time (Fig. 3F). These observations sug-

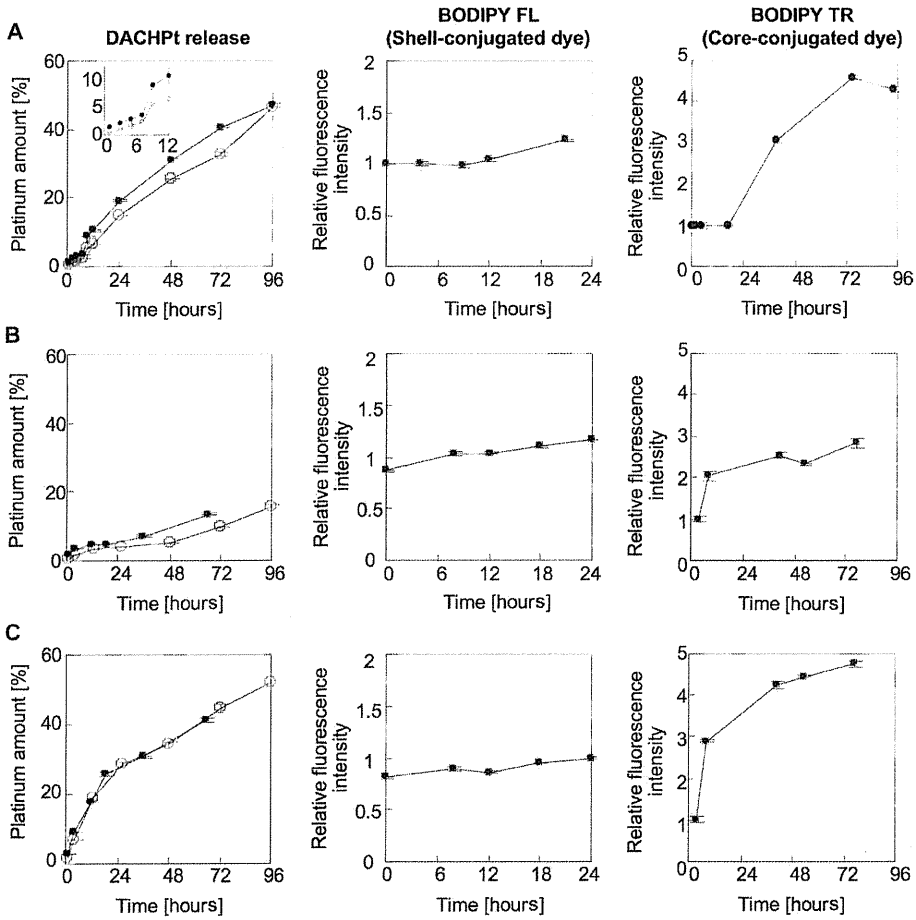

Fig. 2. Properties of F-DACHPt/m under conditions mimicking extracellular and subcellular environments. (**A** to **C**) Release profiles of DACHPt from DACHPt/m and F-DACHPt/m (left column) and fluorescence profiles of BODIPY FL (middle column) and BODIPY TR (right column) under conditions mimicking (A) the extracellular environment (10 mM PBS, pH 7.4, and 150 mM NaCl), (B) the early endosomal environment (10 mM PBS, pH 6.9, and 20 mM NaCl), and (C) the late endosomal environment (10 mM PBS, pH 5.5, and 70 mM NaCl), all at 37°C. Inset in top left panel is the magnification of the profiles of DACHPt release until 12 hours. The release of DACHPt from the micelles was evaluated by dialysis as described in Materials and Methods. Data for DACHPt/m and F-DACHPt/m in the left column are shown as open and filled circles, respectively. Data are expressed as means ± SEM (n = 3).

gested that F-DACHPt/m progressively dissociated in the late endosome and lysosomal compartments. Because these acidic organelles reside in the perinuclear region, F-DACHPt/m would be expected to deliver the active platinum complexes close to the nucleus. Thus, in vitro confocal microscopy revealed that F-DACHPt/m appears to exhibit late endosome/lysosome–selective dissociation concomitant with the release of DACHPt, thereby achieving efficient DACHPt delivery close to the nucleus.

Effect of subcellular pathway on drug efficiency

Oxaliplatin enters the cells by passive diffusion or through copper/organic cation transporters (*29*), and it then changes to active DACHPt aqua complexes in the cytoplasm, some of which may ultimately cross-link with DNA, disrupting DNA function and exerting therapeutic activity (Fig. 1B). However, 75 to 85% of activated platinum drugs are sequestered by abundant sulfur species that serve as cellular defense mechanisms in the cytoplasm, and only 5 to 10% of oxaliplatin can bind to DNA (Fig. 1B) (*30*–*32*). We hypothesized that DACHPt/m facilitates drug delivery close to the nucleus through its perinuclear subcellular localization. Therefore, we studied the pharmacological activity of DACHPt/m. DACHPt/m displayed a value of IC_{50} (the mean concentration that causes 50% growth inhibition) against HT29 cells that was lower than that of oxaliplatin by a factor of 4.7 (Table 1). It is rare that a nanocarrier-encapsulated drug surpasses the free form of the drug for in vitro cytotoxicity (*33*). To elucidate the mechanism of DACHPt/m action, we evaluated the subcellular accumulation of platinum and quantity of Pt-DNA adducts. Exposure of HT29 cells to oxaliplatin resulted in twice as much accumulation of platinum than did exposure to DACHPt/m (Fig. 3G). This is probably because oxaliplatin rapidly enters the cells by diffusion and through copper/organic cation transporters (*29*), whereas DACHPt/m is gradually internalized by endocytosis. Nevertheless, we did not observe a significant difference in the Pt-DNA adducts formed after exposure to oxaliplatin and DACHPt/m (Fig. 3H), indicating that DACHPt/m may efficiently deliver the active platinum drug to DNA (Fig. 3I).

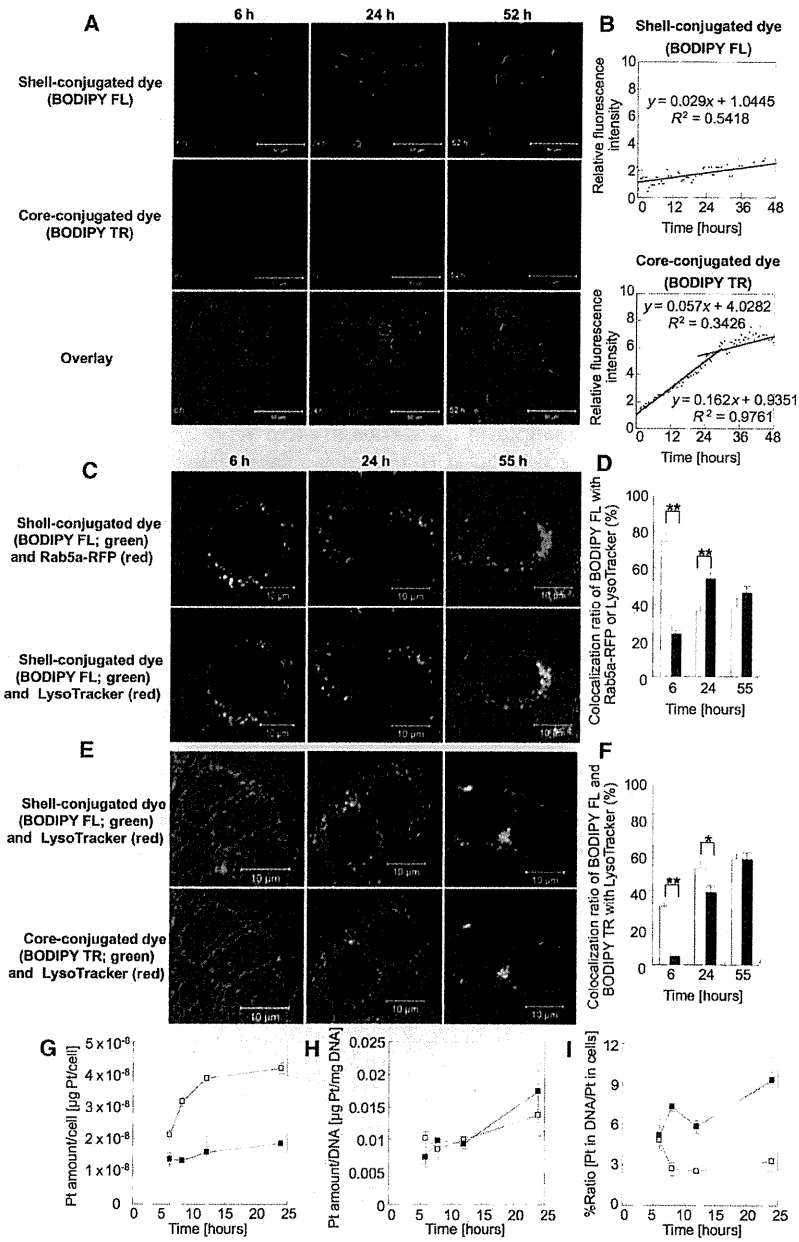

Fig. 3. In vitro observation of subcellular trafficking and fate of F-DACHPt/m, cellular platinum accumulation, and formation of platinum-DNA adducts. (**A**) Representative images of time-lapse CLSM observation of HT29 cells treated with F-DACHPt/m (green, BODIPY FL; red, BODIPY TR; yellow, their colocalization). (**B**) Relative fluorescence intensity of BODIPY FL (upper) and BODIPY TR (lower) of F-DACHPt/m. (**C**) Fluorescent images of colocalization of BODIPY FL of DACHPt/m (green) with an early endosome marker, Rab5a-RFP (red in upper images), or a late endosome and lysosome marker, LysoTracker (red in lower images), in HT29 cells after incubation for 6, 24, and 55 hours. (**D**) Colocalization ratio of BODIPY FL with Rab5a-RFP (open bars) or LysoTracker (closed bars). Data are expressed as means ± SEM ($n = 10$). $^{**}P < 0.01$. (**E**) Fluorescent images of colocalization of BODIPY FL (green in upper images) and BODIPY TR (green in lower images) of F-DACHPt/m with LysoTracker (red) in HT29 cells after incubation for 6, 24, and 55 hours. (**F**) Colocalization ratio of BODIPY FL (open bars) or BODIPY TR (closed bars) with LysoTracker. Data are expressed as means ± SEM ($n = 10$). $^{*}P < 0.05$; $^{**}P < 0.01$. (**G**) In vitro cellular accumulation of platinum. (**H**) DNA platination. (**I**) Ratio of platinum in DNA to total platinum in cells expressed as a percentage. DNA platination was converted from μg Pt/mg DNA to μg Pt/cell, and the ratio was calculated. Open squares, oxaliplatin; filled squares, DACHPt/m. Data are expressed as means ± SEM ($n = 3$).

We also evaluated the mean concentration required for 50% growth inhibition (GI_{50}), which is defined as in (*34, 35*), in a human cell panel composed of 37 cancer cell lines (fig. S5), and investigated the correlation between GI_{50} and expression of 26 genes that we selected on the basis of their potential association with the pharmacological activity of platinum compounds (*36*). The cytotoxic activity of oxaliplatin was inversely correlated with the expression of metallothionein (MT1Q) and methionine synthase (MTR), which are found in the cytoplasm and inactivate platinum compounds. DACHPt/m cytotoxicity did not exhibit similar correlations (table S1). We conclude that DACHPt/m may bypass cytoplasmic detoxification by MTR and MT1Q and efficiently deliver active platinum complexes to the nucleus, because they are internalized by endocytosis and selectively release the active platinum complexes in the late endosome/lysosome compartment (Fig. 1B).

Effect of DACHPt/m on oxaliplatin resistance in vitro

Our proposed mechanism of action of DACHPt/m led us to investigate their efficacy in oxaliplatin-resistant cancer cells, because MTR and MT1Q are overexpressed in these cells (*37–39*). We developed oxaliplatin-resistant HT29 cells (HT29/ox) by chronic exposure of HT29 cells to oxaliplatin with gradual dose escalation. Relative to the parental HT29 cells, HT29/ox cells were 10 times as resistant to oxaliplatin (Table 1). Quantitative real-time reverse transcription polymerase chain reaction (RT-PCR) and Western blotting revealed that the HT29/ox cells showed up-regulated messenger RNA (mRNA) as well as protein for MTR and MT1Q compared with HT29 cells (Fig. 4, A and B). Moreover, the down-regulation of MT1Q and MTR with small interfering RNA (siRNA) restored the sensitivity of HT29/ox cells to oxaliplatin (fig. S6). In vitro cytotoxicity studies showed that DACHPt/m was 120 times as cytotoxic as oxaliplatin in HT29/ox cells (Table 1). These results suggested that DACHPt/m may overcome acquired resistance to oxaliplatin.

In vivo intratumoral imaging of F-DACHPt/m in a human colon cancer model

DACHPt/m would need to extravasate, penetrate into the interstitial tissue, and be internalized by cancer cells after systemic administration to exert the in vivo antitumor activity predicted from the results above. We performed real-time intravital observation of the accumulation and subcellular fate of F-DACHPt/m in HT29 xenografts by using in vivo CLSM equipped with a high-speed resonant scanner developed to acquire live tissue images of experimental animals (fig. S7). Immediately after intravenous injection, F-DACHPt/m was observed in the blood vessels of solid tumors (Fig. 5A and video S2). The fluorescence from F-DACHPt/m in the blood vessels corresponded only to that of BODIPY FL. Even 12 hours later, only BODIPY FL fluorescence was observed flowing in the blood vessels (Fig. 5B and video S3). These observations indicate that F-DACHPt/m stably circulates in the bloodstream while maintaining their micellar structure. Images of tumor tissue revealed the accumulation and dissociation behaviors of F-DACHPt/m (Fig. 5, C and D, and video S3). Two hours after injection, F-DACHPt/m accumulated within the tumor tissue because of the EPR effect and was identified within the cells, whereas BODIPY TR fluorescence remained quenched. BODIPY TR fluorescence gradually appeared inside the cells 4 hours after injection and was clearly visible after 12 hours, indicating the release of DACHPt

Table 1. In vitro cytotoxicity of free oxaliplatin and DACHPt/m against HT29 and HT29/ox cells after a 48-hour incubation. Data are expressed as means ± SEM (n = 4).

Cells	IC_{50} (μM)*		
	Free oxaliplatin	DACHPt/m	Oxaliplatin/ DACHPt/m
HT29	2.2 ± 2.2	0.47 ± 0.05	4.7
HT29/ox	22.8 ± 2.6	0.19 ± 0.11	120
Ratio of HT29/ox/HT29	10.4	0.4	—

*IC_{50} values obtained from the MTT assay.

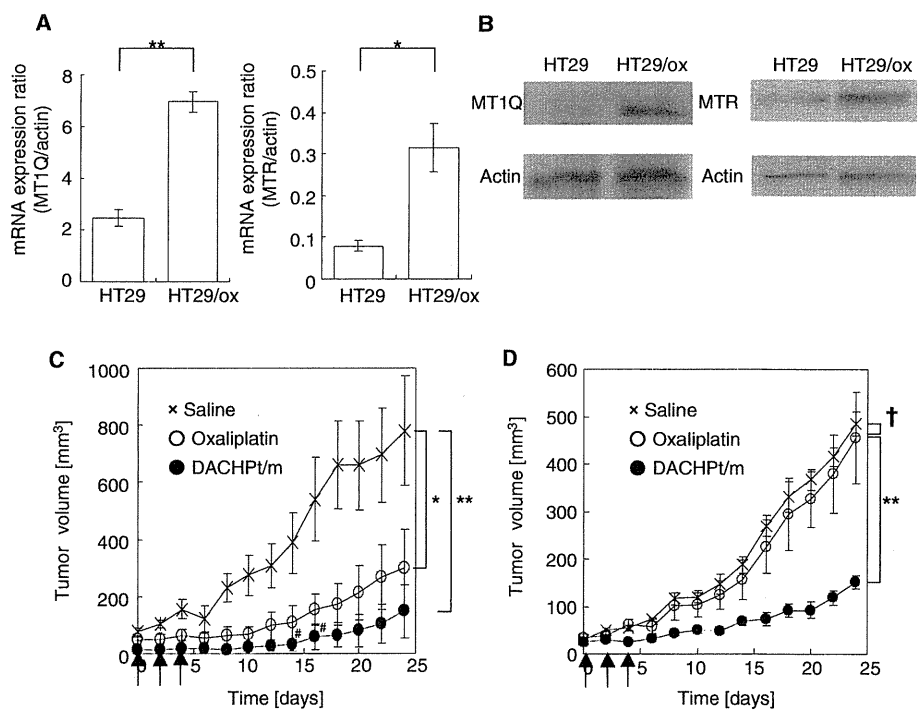

Fig. 4. Expression of MT1Q and MTR in HT29/ox cells and effects of DACHPt/m on HT29 and HT29/ox tumors in vivo. (**A**) Relative mRNA expression of metallothionein (MT1Q) and methionine synthase (MTR) in parent HT29 and HT29/ox cell lines. Data are expressed as means ± SEM (n = 3). *P < 0.05; **P < 0.01. (**B**) Western blots of MT1Q and MTR in HT29 and HT29/ox cell lines. (**C** and **D**) In vivo effect of DACHPt/m on subcutaneous HT29 (C) and HT29/ox (D) tumor cells. Crosses, saline; open circles, oxaliplatin (8 mg/kg); filled circles, DACHPt/m (4 mg/kg); arrows, injection of oxaliplatin and DACHPt/m; #, tumor regression; †P > 0.1; *P < 0.05; **P < 0.01. Data are expressed as means ± SEM (n = 4).

from the micelles inside the cells in the tumor tissue. The cell membrane, stained with CellMask, and cell nuclei were substantially free of F-DACHPt/m (Fig. 5, C and D, and video S3). These results were consistent with our in vitro results (Fig. 3A) and suggested that F-DACHPt/m percolated into interstitial tissues and was efficiently internalized to endosomal compartments of cells in a micelle form, followed by dissociation of the multimolecular structure of the micelles in the late endosomal and lysosomal compartments.

DACHPt/m enhances antitumor activity and overcomes oxaliplatin resistance in vivo

On the basis of our observations of the in vivo behavior of F-DACHPt/m, we hypothesized that DACHPt/m may also overcome oxaliplatin resistance in vivo. Thus, we evaluated DACHPt/m in vivo antitumor activity against subcutaneous HT29 and HT29/ox tumors (Fig. 4, C and D). Although free oxaliplatin failed to inhibit the growth of HT29/ox tumors, DACHPt/m exhibited substantial antitumor activity in the oxaliplatin-resistant xenograft model and successfully overcame the oxaliplatin resistance of HT29/ox cells in vivo (Fig. 4D). Note that DACHPt/m also achieved higher antitumor activity than oxaliplatin against the HT29 tumors (Fig. 4C). Thus, our micelle-based drug delivery vehicle was able to circumvent the detoxification mechanisms against platinum drugs in tumor cell cytoplasm through selective subcellular drug release and hence overcome acquired resistance.

DISCUSSION

Colorectal cancer is a major cause of morbidity and mortality worldwide (*1*). Oxaliplatin is currently the standard therapy for colorectal cancer, and acquired resistance to oxaliplatin is a major clinical drawback in the treatment of colorectal cancer [virtually all metastatic colorectal cancer becomes resistant to oxaliplatin, with a median time to progression of 8.7 months (*40*)]. The major cellular processes by which oxaliplatin enters and attacks cancer cells include uptake and transport, formation of DNA adducts and their recognition by damage response proteins, and signal transduction leading to apoptosis. Any factors that interfere with these pathways can lead to drug resistance (*41*). Here, we showed that DACHPt/m can overcome drug resistance by circumventing recognition by MTR and MT1Q, and achieve subcellular drug delivery both in vitro and in vivo to the perinuclear region of cells. It has been reported that drug delivery systems can overcome multidrug resistance

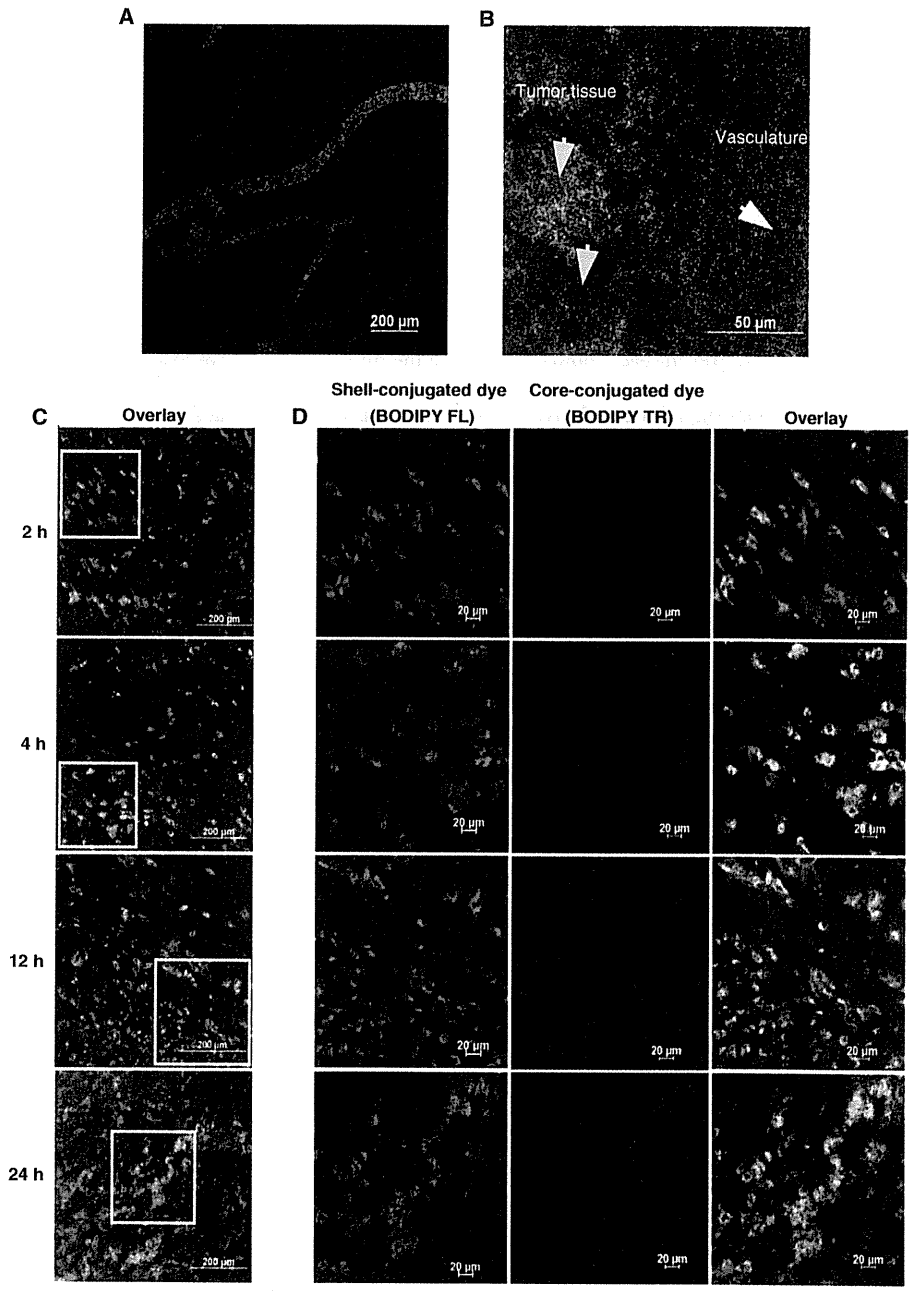

Fig. 5. In vivo CLSM observation of F-DACHPt/m in blood vessels and tumors after intravenous administration. (**A** and **B**) CLSM observation of F-DACHPt/m in the blood vessels of solid tumors (A) immediately after injection and (B) in the tumor tissue at 12 hours after injection. Yellow arrows, tumor tissue; white arrow, blood vessel. (**C**) Time-dependent CLSM observation of F-DACHPt/m in the tumor tissues at 2, 4, 12, and 24 hours after injection. Green, fluorescence from the shell-conjugated dyes (BODIPY FL); red, core-conjugated dyes (BODIPY TR); blue, cell surfaces stained by CellMask. (**D**) Magnification of selected areas [square regions in (C)] by channel.

by avoiding the drug efflux mechanism of P-glycoprotein (*20–22*). Because P-glycoprotein is not associated with platinum drug resistance (*42*), we used a different approach. Our data indicate that cytoplasmic detoxification mechanisms against platinum drugs can potentially be avoided by using the appropriate drug delivery system.

Nanocarriers encounter numerous barriers in vivo en route to their target during the processes of blood circulation, extravasation, penetration, and cellular uptake. It is therefore difficult to extrapolate in vivo outcomes of a drug-nanocarrier combination from its in vitro behavior, although real-time observation of in vivo behaviors such as we have used here can ascertain critical barriers residing in a living body and facilitate the design of a nanocarrier optimized for in vivo delivery. The in vivo CLSM technique that we used in this study enabled spatiotemporal and quantitative analyses of extravasation, tissue penetration, and cellular internalization of nanocarriers in living animals. Using dual fluorescent labeling of DACHPt/m, we elucidated the real-time intratumoral behavior of DACHPt/m. The dual fluorescent label of DACHPt micelles allowed us to trace the micelles' position by the ever-present fluorescent signal from the surface of the micelles, and the drug release and dissociation of the multimolecular structure of the micelles by the dequenching and fluorescence recovery of the core-conjugated dye. In in vitro cellular experiments, these micelles were internalized intact, and then they were disassembled and the drug was released in late endosomes. In our in vivo microscopy, we observed that DACHPt/m maintained their micelle form during circulation in the blood, probably because of the stable inner core structure formed by the polymer-metal complexes, and extravasated into solid tumors. DACHPt/m was able to deeply penetrate cancerous tissue after extravasation and was internalized by different cell populations that were distant from the blood vessels. Such efficient penetration of tissue is a requirement of successful drug delivery and a prerequisite for effective subcellular targeting. It has been reported that PEG-modified liposomes with 100-nm diameter accumulated at perivascular regions of solid tumors and failed to penetrate the tumor interstitium deeply (*43*). Although this characteristic may depend on the cancer type, it is possible that the deep tumor penetration of DACHPt/m is a result of their smaller 30-nm size. Finally, the DACHPt/m structure dissociated at the perinuclear regions of the cell after internalization, based on the pH and chloride ion concentration–selective release of DACHPt. This observation is also consistent with our hypothesis that DACHPt/m can overcome oxaliplatin resistance in tumors by bypassing the cytoplasmic detoxification mechanisms of MTR and MT1Q. There are, however, several limitations to the type of study that we have performed in a subcutaneous tumor model. Compared with subcutaneous tumors, orthotopic and spontaneously forming tumors may have characteristic differences such as vascular density and degree of fibrosis, which may affect the transport of nanocarriers (*44*).

Our research provides one approach for subcellular targeting of cytoplasmic drugs. Such nanocarriers have the potential to enhance the drug efficacy and overcome drug resistance.

MATERIALS AND METHODS

Materials

γ-Benzyl L-glutamate and bis(trichloromethyl) carbonate (triphosgene) were purchased from Sigma Chemical and Tokyo Kasei Kogyo, respectively. *N,N*-Dimethylformamide (DMF), 3-(4,5-dimethylthiazol-2-yl)-2,5-diphenyltetrazolium bromide (MTT), and dimethyl sulfoxide (DMSO) were purchased from Wako Pure Chemicals. Oxaliplatin and $NaCH_3CN$ were purchased from Sigma-Aldrich Inc. Dichloro(1,2-diammino cyclohexane) platinum(II) was purchased from W. C. Heraeus GmbH. α-Methoxy-ω-amino-poly(ethylene glycol) [CH_3O-PEG-NH_2; molecular weight (MW), 12,000] was purchased from Nippon Oil and Fats. BODIPY TR-succinimidyl ester, BODIPY FL-hydrazide, LysoTracker Blue, CellLight Early Endosome-RFP (Rab5a-RFP), CellMask, and Lipofectamine RNAiMAX were purchased from Invitrogen.

Cell lines and animals

HT29 cells were purchased from the American Type Culture Collection. HT29 cells were maintained in McCoy's 5A modified medium (Invitrogen) containing 10% fetal bovine serum (Gibco) as well as 1% penicillin and streptomycin (Sigma) and were cultured at 37°C in a humidified atmosphere of 5% CO_2. To develop HT29/ox cells (*45*), we treated HT29 cells with oxaliplatin at IC_{50} doses for 1 hour. After 24 hours, cells were subcultured into new flasks and oxaliplatin was added to a culture of 80% confluent cells. The concentration was incrementally increased by factors of 1.2 to 2. The process was continued until the cells were resistant to drug concentrations at least 10 times as great. BALB/c-nu/nu mice (female; body weight, 18 to 20 g; age, 6 weeks old) were purchased from Charles River Japan. All animal experiments were carried out in accordance with the guidelines for animal experiments at the University of Tokyo, Japan.

Methods

Synthesis of block copolymers. α-4-(Diethoxymethyl)benzyl-ω-amino-poly(ethylene glycol) (Ac-Bz-PEG-NH_2) was previously synthesized in our laboratory (*46*). Poly(ethylene glycol)-*b*-poly(L-glutamic acid) [PEG-*b*-P(Glu)] [MW_{PEG}, 12,000; polymerization degree of P(Glu), 20] and Ac-Bz-PEG-*b*-poly(L-glutamic acid) [Ac-Bz-PEG-*b*-P(Glu)] [MW_{PEG}, 12,000; polymerization degree of P(Glu), 20] were synthesized according to the previously described synthetic method (*47*). Briefly, *N*-carboxyanhydride of γ-benzyl L-glutamate (BLG-NCA) was synthesized by the Fuchs-Farthing method with triphosgene (*48*). BLG-NCA was polymerized in DMF initiated by the amino group of CH_3O-PEG-NH_2 or Ac-Bz-PEG-NH_2 to obtain PEG-*b*-poly(γ-benzyl L-glutamate) (PEG-*b*-PBLG) or Ac-Bz-PEG-*b*-PBLG, respectively. The MW distribution of PEG-*b*-PBLG and Ac-Bz-PEG-*b*-PBLG was determined by gel permeation chromatography (GPC) [column, TSK-gel G3000HHR, G4000HHR (Tosoh); eluent, DMF containing 10 mM LiCl; flow rate, 0.8 ml/min; detector, refractive index; temperature, 25°C]. PEG-*b*-PBLG and Ac-Bz-PEG-*b*-PBLG showed narrow MW distributions (M_w/M_n: 1.09 and 1.16, respectively) in GPC. The degrees of polymerization of PBLG in PEG-*b*-PBLG and Ac-Bz-PEG-*b*-PBLG were determined to be 20 by comparing the proton ratios of methylene units in PEG (-OCH_2CH_2-: δ = 3.7 ppm) and phenyl groups of PBLG (-$CH_2C_6H_5$: δ = 7.3 ppm) in ^{1}H-NMR (nuclear magnetic resonance) measurement. Both PEG-*b*-PBLG and Ac-Bz-PEG-*b*-PBLG were deprotected by mixing with 0.5 N NaOH at room temperature to obtain PEG-*b*-P(Glu) and Ac-Bz-PEG-*b*-P(Glu), respectively. Complete deprotection was confirmed by ^{1}H NMR measurement.

Preparation of micelles. For conjugation of BODIPY TR to a polymer, a solution of BODIPY TR-succinimidyl ester in DMSO (1 mg/ml) was mixed with Ac-Bz-PEG-*b*-P(Glu). The reaction was carried out overnight at room temperature with stirring. Unreacted

BODIPY TR was removed by dialysis [MW cutoff (MWCO) size, 2000 daltons] against DMSO and water. To conjugate BODIPY FL to the Ac-Bz-PEG-*b*-P(Glu)-BODIPY TR polymer, we mixed a solution of BODIPY FL-hydrazide in DMSO with the polymer, followed by the addition of 1 N HCl to deprotect the acetal group. Samples were stirred overnight at room temperature and treated with $NaBH_3CN$ to reduce the link between BODIPY FL and the polymer. For purification, unbound BODIPY FL was removed by dialysis (MWCO, 2000 daltons) against DMSO and water. The prepared BODIPY FL-PEG-*b*-P(Glu)-BODIPY TR copolymer was freeze-dried overnight and stored at −20°C. DACHPt/m and F-DACHPt/m were prepared according to the previously described method (*23*). DACHPt (5 mM) was suspended in distilled water and mixed with silver nitrate ([$AgNO_3$]/[DACHPt] = 1) to form aqueous complexes. The solution was kept in the dark at 25°C for 24 hours. AgCl precipitates were eliminated by centrifugation. The supernatant was purified by passage through a 0.22-μm filter. DACHPt aqueous complex solution was then mixed with PEG-*b*-P(Glu) or BODIPY FL-PEG-*b*-P(Glu)-BODIPY TR ([Glu] = 5 mM; [DACHPt]/[Glu] = 1.0) and reacted for 120 hours to obtain DACHPt/m or F-DACHPt/m, respectively. DACHPt/m and F-DACHPt/m were purified by ultrafiltration (MWCO, 30,000 daltons; Fig. 1A). The size distributions of DACHPt/m and F-DACHPt/m were evaluated by dynamic light scattering at 25°C with a Zetasizer Nano ZS90 (Malvern Instruments). The platinum content of DACHPt/m was determined by ion-coupled plasma mass spectrometry (4500 ICP-MS; Hewlett Packard).

Drug release and fluorescence profiles of micelles under different conditions. The release of platinum from DACHPt/m and F-DACHPt/m in phosphate-buffered saline (PBS) at 37°C was evaluated as described (*23*). Briefly, a micelle solution of known platinum concentration was placed inside a dialysis bag (MWCO, 2000 daltons). The solution was then dialyzed against PBS under different conditions mimicking the extracellular environment (10 mM PBS, pH 7.4, and 150 mM NaCl), early endosomes (10 mM PBS, pH 6.9, and 20 mM NaCl), and late endosomes (10 mM PBS, pH 5.5, and 70 mM NaCl) at 37°C (*25*). The concentration of platinum present in the dialysate was determined with ICP-MS. The fluorescence profiles of F-DACHPt/m were also evaluated under the same conditions with a spectrofluorometer (FP6600, Jasco) or NanoDrop (ND3300, Scrum). Changes in fluorescence intensity were measured at a defined time period.

In vitro observation of subcellular localization and the fate of F-DACHPt/m by CLSM. HT29 cells were cultured at 1×10^5 cells in 35-mm glass-based dishes (Asahi Techno Glass). After overnight incubation in a fresh medium, the cells were washed twice with PBS. The medium was then replaced by 1 ml of fresh medium containing F-DACHPt/m (100 μM on Pt base). Live-cell CLSM imaging was performed with a Zeiss LSM 510 META nonlinear optics scan head attached to an inverted Axiovert 200 M SP equipped with a 63 × 1.4 numerical aperture Plan Apochromat oil immersion objective (Carl Zeiss). For long-term time-lapse imaging, culture dishes were wrapped with an optically clear foil cover (Carl Zeiss) to avoid evaporation and mounted onto the microscope stage incubator (37°C, 5% CO_2, 90% relative humidity). Bright-field DIC (differential interference contrast) images and fluorescent sequences were taken every 30 min for 72 hours. BODIPY FL was excited at 488 nm with an Ar laser and fluorescence was detected at 500 to 530 nm, whereas BODIPY TR was excited at 543 nm with a He-Ne laser, and fluorescence was detected at 565 to 615 nm. Laser power was kept low at 0.36 mW for 488 nm and at 0.018 mW for 543 nm so that photobleaching was negligible. To determine whether DACHPt/m was taken up by endocytosis, we treated HT29 cells with F-DACHPt/m at 37°C or 4°C for 6 hours and then observed by CLSM. For the colocalization studies, we used micelles prepared from BODIPY FL-PEG-P(Glu) that only emit fluorescence from the shell. HT29 cells, which had been preincubated with CellLight Early Endosome-RFP to express an early endosome marker, Rab5a-RFP, were treated with BODIPY FL–conjugated DACHPt/m, and images were taken at indicated time points after staining with LysoTracker Blue. Rab5a-RFP was excited at 543 nm with a He-Ne laser, and fluorescence was detected at 565 to 615 nm. LysoTracker Blue was excited in multiphoton mode at 710 nm with a Mai Tai tunable broadband laser (Spectra-Physics), and fluorescence was detected at 390 to 465 nm. Colocalization was quantified as follows:

$$\text{amount of colocalization (\%)} = \text{BODIPY FL pixels}_{\text{colocalization}}/\text{BODIPY FL pixels}_{\text{total}} \times 100$$

where BODIPY FL $\text{pixels}_{\text{colocalization}}$ represents the number of BODIPY FL pixels colocalizing with Rab5a-RFP or LysoTracker pixels in the cytoplasm, and BODIPY FL $\text{pixels}_{\text{total}}$ represents the number of all BODIPY FL pixels in the cytoplasm. The timing and location of the micelle dissociation and concomitant drug release were studied by evaluating the colocalization of BODIPY FL and BODIPY TR signals from F-DACHPt/m with the late endosomes/lysosomes (Fig. 3, E and F). Cells were treated with F-DACHPt/m, and images were taken at indicated time points after staining with LysoTracker Blue. Colocalization was quantified as follows:

$$\text{amount of colocalization (\%)} = \text{BODIPY FL or BODIPY TR pixels}_{\text{colocalization}}/\text{BODIPY FL or BODIPY TR pixels}_{\text{total}} \times 100$$

where BODIPY FL or BODIPY TR $\text{pixels}_{\text{colocalization}}$ represents the number of BODIPY FL or BODIPY TR pixels colocalizing with LysoTracker pixels in the cytoplasm, and BODIPY FL or BODIPY TR $\text{pixels}_{\text{total}}$ represents the number of all BODIPY FL or BODIPY TR pixels in the cytoplasm.

Determination of subcellular Pt accumulation and amount of Pt-DNA adducts. HT29 cells (6×10^6) were seeded in 100-mm tissue culture dishes. After 24 hours, cells were treated with 10 μM oxaliplatin or DACHPt/m on a platinum base. After 6, 8, 12, and 24 hours of drug exposure, the medium was removed and the cells were washed three times with PBS, scraped, and harvested. Samples were freeze-dried overnight, dissolved in heated nitric acid, and evaporated to dryness. The samples were redissolved in water and the Pt content was determined by ICP-MS. For the quantification of Pt-DNA adducts, DNA was extracted with a DNA purification kit (Promega) according to the manufacturer's protocol. The amount and purity of DNA were determined by measuring absorption at 260 and 280 nm with NanoDrop (ND3300). The DNA was dissolved in nitric acid, dried, and redissolved in water. The Pt content was determined by ICP-MS, and the DNA platination levels were expressed as micrograms of Pt per milligram of DNA.

In vitro cytotoxicity study against human cancer cells. The in vitro cytotoxicity of oxaliplatin and DACHPt/m was examined against a panel of 37 human cancer cells as described (*34*, *35*). Cancer cells were plated into flat-bottomed 96-well plates at 5×10^3 per well. Cells were treated by continuous exposure to oxaliplatin or DACHPt/m in a final volume of 100 μl. Plates were incubated for 48 hours at 37°C in a humidified atmosphere with 5% CO_2, and cell viability was determined

by MTT assay. To determine the relationship between cellular sensitivity to oxaliplatin or DACHPt/m and the expression of genes involved in the sensitivity or resistance of cells to platinum compounds, we assessed the gene expression profile of 21 human cancer cell lines for 26 genes selected on the basis of previous studies on cisplatin- or oxaliplatin-resistant cells (*36*). Expression of these individual genes was determined by searching the National Cancer Institute database. The coefficient of correlation between the GI_{50}s of free oxaliplatin and DACHPt/m as well as the level of gene expression was calculated for each gene.

Quantitative real-time RT-PCR. The expression of the metallothionein (MT1Q) [human MT1B (same as MT1Q), NM_005947, 4MQ-012725-01-0002] and methionine synthase (MTR) (human MTR, NM_000254, 4LQ-009896-00-0002) was confirmed by quantitative real-time RT-PCR. After 24 hours of treatment, cells were washed with PBS and harvested. Total RNA was prepared with TRIzol (Invitrogen), and complementary DNA (cDNA) was reverse-transcribed with a QuantiTect reverse transcription kit (Qiagen). PCR primer sequences were as follows: MT1Q, 5′-GAACTCCAGGCTTGTCTTGG-3′ (forward) and 5′-CATTTGCACTCTTTGCACTTG-3′ (reverse); MTR, 5′-ACCCAACTTCCAGGGAGACT-3′ (forward) and 5′-GGCAC-CATGATCTTGGACTT-3′ (reverse); actin, 5′-AGATGTGGATCAG-CAAGCAG-3′ (forward) and 5′-GCGCAAGTTAGGTTTTGTCA-3′ (reverse); and 18S, 5′-CGGCGACGACCCATTCGAAC-3′ (forward) and 5′-GAATCGAACCCTGATTCCCCGTC-3′ (reverse). cDNA from HT29 cells was amplified with specific primers with a SYBR Green Core Reagent Kit (Qiagen) and a real-time PCR instrument (Applied Biosystems). Expression of each gene was standardized with endogenous actin or 18*S* as a control, and its relative levels in HT29 or HT29/ox cells were quantified by calculating $2^{-\Delta\Delta C_T}$, where $\Delta\Delta C_T$ is the difference in C_T (cycle number at which the amount of amplified target reaches a fixed threshold) between target and reference.

MT1Q and MTR gene knockdown. The siRNAs against MT1Q and MTR and the control siRNA were purchased from Thermo Fisher Scientific Inc. The siRNA target sequences against MT1Q are the following: siMT1Q, GCAAAGGCUCAUCAGAGAA. The siRNA sequences against MTR are the following: siMTR, CUGAGAAGCU-CUUACGUUA. The siRNAs were transfected into the cell with Lipofectamine RNAiMAX (Invitrogen) according to the instructions of the manufacturer. Briefly, HT29/ox cells (4×10^5) were seeded in six-well plates. Twenty-four hours later, the mixture of siMT1Q (50 nM) and siMTR (50 nM) was transfected into the cells with Lipofectamine RNAiMAX reagent. Knockdown of MT1Q and MTR was separately confirmed by real-time PCR (fig. S6, A and B, respectively). To investigate the role of MT1Q and MTR in the oxaliplatin resistance in HT29/ox cells, we seeded HT29/ox cells (5×10^3) in 96-well plates, and 24 hours later, the mixture of siMT1Q (50 nM) and siMTR (50 nM) or the control siRNA was transfected into the cells with Lipofectamine RNAiMAX reagent. Twenty-four hours after transfection, the transfected HT29/ox cells were treated by continuous exposure to oxaliplatin in a final volume of 100 μl. Plates were further incubated for 48 hours at 37°C in a humidified atmosphere with 5% CO_2, and their cytotoxicity was determined by MTT assay.

Western blotting. HT29 or HT29/ox cells (5×10^6) were seeded in 100-mm^2 plates and washed with PBS (100 μl). Cell extracts were resolved in TNE buffer [1% NP-40, 150 mM NaCl, 10 mM tris-HCl, 1 mM EDTA, aprotinin (10 μg/ml), 2 mM Na_3VO_4, 10 mM NaF]. The cell suspension was centrifuged for 20 min at 15,000*g*. Sampling buffer (4×) was added to the aliquots, followed by incubation for 5 min at 100°C. Transfer to a polyvinylidene difluoride membrane (Invitrogen) was performed by electrophoresis for 90 min at 125 V. Membranes were blocked with 6% nonfat milk or tris-buffered saline (TBS) with 0.1% Tween 20 (MT1Q) for 1 hour. They were then probed at room temperature with the following antibodies: anti-metallothionein (ab12228, 1:1000, Abcam), anti–methionine synthase (ab66039, 1:2000, Abcam), and anti–β-actin (#4967, 1:1000, Cell Signaling). Membranes were washed three times with washing buffer (TBS with 0.1% Tween 20) and then probed with the secondary anti–rabbit immunoglobulin G (IgG) horseradish peroxidase (HRP) (W401B, 1:10,000, Promega) or anti–mouse IgG HRP (W402B, 1:10,000, Promega) conjugate for 1 hour. The secondary antibody was washed three times with washing buffer and then evenly coated with enhanced chemiluminescence (ECL) Western blotting detection reagents (GE Healthcare) for 30 s. The membrane was immediately exposed to Fuji Medical X-ray film (Fujifilm) at room temperature for various periods in a film cassette. Protein levels were standardized with the signal from the β-actin probe.

In vivo antitumor activity studies. BALB/c-nu/nu mice (female, $n = 4$) were inoculated subcutaneously with HT29 or HT29/ox cells (1×10^7/ml). Tumors were allowed to grow for 1 week (tumor size at this point was about 40 mm^3). Mice were then treated intravenously three times at 2-day intervals with oxaliplatin (8 mg/kg) or DACHPt/m (4 mg/kg) on a platinum base. Antitumor activity was evaluated in terms of tumor size (V) with the following equation:

$$V = a \times b^2/2$$

Here, a and b are the major and minor axes, respectively, of the tumor as measured by a caliper.

Intravital observation of the in vivo behavior of F-DACHPt/m. Intravital observation of F-DACHPt/m was performed as described (*49*). Female BALB/c mice (6 to 8 weeks old) were inoculated subcutaneously with HT29 cells (1×10^7/ml). After 5 days, when the tumor volumes reached 70 mm^3, F-DACHPt/m (10 mg/kg) was administered intravenously. At 2, 4, 12, and 24 hours after treatment, mice were anesthetized with 2.5% isoflurane (Abbott Japan) with a Univentor 400 Anesthesia Unit (Univentor). An arc-shaped incision was made around the subcutaneous tumor, and the skin flap was elevated without injuring the feeding vessels. The mouse was placed directly onto a thermoplate (Tokai Hit), and the skin flap was everted and stretched with several bent 30-gauge needles. The plasma membrane stain, CellMask Deep Red, was directly applied to the subcutaneous tumor, and a coverslip (Muto Pure Chemicals) was attached with just enough pressure to flatten the tumor surface. All in vivo images were acquired with a Nikon A1R CLSM attached to an upright Eclipse FN1 (Nikon). The A1R incorporates a conventional galvano scanner and a high-speed resonant scanner. The latter allows an acquisition speed of 30 frames per second while maintaining a relatively high resolution of 512 × 512 scanned points. BODIPY FL, BODIPY TR, and CellMask were excited with three lasers (488-nm Ar, 560-nm He-Ne, and 640-nm He-Ne lasers), and the fluorescent signals were detected. Laser powers were kept at 19.5 mW for 488-nm Ar, 7.5 mW for 561-nm He-Ne, and 1 mW for 640-nm He-Ne.

Statistical analysis. Data are presented as means ± SEM. The significant differences between the groups were analyzed by a Student's t test, and a P value of <0.05 was considered significant.

SUPPLEMENTARY MATERIAL

www.sciencetranslationalmedicine.org/cgi/content/full/3/64/64ra2/DC1
Fig. S1. Synthetic scheme of BODIPY FL-PEG-*b*-P(Glu)-BODIPY TR.
Fig. S2. Size distribution of DACHPt/m and F-DACHPt/m as determined by dynamic light scattering.
Fig. S3. Fluorescent images of HT29 cells after 6-hour incubation with F-DACHPt/m at 37°C and 4°C.
Fig. S4. In vitro CLSM observation of dissociation of F-DACHPt/m in the late endosomes/lysosomes.
Fig. S5. In vitro cytotoxicity of oxaliplatin and DACHPt/m against a human cancer cell panel.
Fig. S6. Knockdown of MT1Q and MTR restores the sensitivity of HT29/ox to oxaliplatin.
Fig. S7. Schematic illustration of experimental settings of in vivo CLSM.
Table S1. Coefficient of correlation between the GI_{50}s of free oxaliplatin or DACHPt/m and the expression levels of genes involved in the sensitivity or resistance of cells to platinum compounds.
Video S1. In vitro live imaging.
Video S2. In vivo live imaging (immediately after injection).
Video S3. In vivo live imaging (12 hours after injection).

REFERENCES AND NOTES

1. A. Jemal, R. Siegel, E. Ward, Y. Hao, J. Xu, M. J. Thun, Cancer statistics, 2009. *CA Cancer J. Clin.* **59**, 225–249 (2009).
2. T. M. Allen, P. R. Cullis, Drug delivery systems: Entering the mainstream. *Science* **303**, 1818–1822 (2004).
3. M. Ferrari, Cancer nanotechnology: Opportunities and challenges. *Nat. Rev. Cancer* **5**, 161–171 (2005).
4. V. P. Torchilin, Recent advances with liposomes as pharmaceutical carriers. *Nat. Rev. Drug Discov.* **4**, 145–160 (2005).
5. R. Duncan, The dawning era of polymer therapeutics. *Nat. Rev. Drug Discov.* **2**, 347–360 (2003).
6. Y. Matsumura, H. Maeda, A new concept for macromolecular therapeutics in cancer chemotherapy: Mechanism of tumoritropic accumulation of proteins and the antitumor agent Smancs. *Cancer Res.* **46**, 6387–6392 (1986).
7. M. E. Davis, Z. G. Chen, D. M. Shin, Nanoparticle therapeutics: An emerging treatment modality for cancer. *Nat. Rev. Drug Discov.* **7**, 771–782 (2008).
8. N. Nishiyama, K. Kataoka, Current state, achievements, and future prospects of polymeric micelles as nanocarriers for drug and gene delivery. *Pharmacol. Ther.* **112**, 630–648 (2006).
9. M. Yokoyama, M. Miyauchi, N. Yamada, T. Okano, Y. Sakurai, K. Kataoka, S. Inoue, Characterization and anticancer activity of the micelle-forming polymeric anticancer drug adriamycin-conjugated poly(ethylene glycol)-poly(aspartic acid) block copolymer. *Cancer Res.* **50**, 1693–1700 (1990).
10. K. Kataoka, G. S. Kwon, M. Yokoyama, T. Okano, Y. Sakurai, Block copolymer micelles as vehicles for drug delivery. *J. Control. Release* **24**, 119–132 (1993).
11. K. Kataoka, A. Harada, Y. Nagasaki, Block copolymer micelles for drug delivery: Design, characterization and biological significance. *Adv. Drug Deliv. Rev.* **47**, 113–131 (2001).
12. A. V. Kabanov, E. V. Batrakova, D. W. Miller, Pluronic block copolymers as modulators of drug efflux transporter activity in the blood–brain barrier. *Adv. Drug Deliv. Rev.* **55**, 151–164 (2003).
13. Y. Matsumura, K. Kataoka, Preclinical and clinical studies of anticancer agent-incorporating polymer micelles. *Cancer Sci.* **100**, 572–579 (2009).
14. Y. Matsumura, T. Hamaguchi, T. Ura, K. Muro, Y. Yamada, Y. Shimada, K. Shirao, T. Okusaka, H. Ueno, M. Ikeda, N. Watanabe, Phase I clinical trial and pharmacokinetic evaluation of NK911, a micelle-encapsulated doxorubicin. *Br. J. Cancer* **91**, 1775–1781 (2004).
15. T. Hamaguchi, K. Kato, H. Yasui, C. Morizane, M. Ikeda, H. Ueno, K. Muro, Y. Yamada, T. Okusaka, K. Shirao, Y. Shimada, H. Nakahama, Y. Matsumura, A phase I and pharmacokinetic study of NK105, a paclitaxel-incorporating micellar nanoparticle formulation. *Br. J. Cancer* **97**, 170–176 (2007).
16. T. Hamaguchi, T. Doi, T. Eguchi-Nakajima, K. Kato, Y. Yamada, Y. Shimada, N. Fuse, A. Ohtsu, S. Matsumoto, M. Takanashi, Y. Matsumura, Phase I study of NK012, a novel SN-38–incorporating micellar nanoparticle, in adult patients with solid tumors. *Clin. Cancer Res.* **16**, 5058–5066 (2010).
17. R. H. Wilson, R. Plummer, J. Adam, M. M. Eatock, A. V. Boddy, M. Griffin, R. Miller, Y. Matsumura, T. Shimizu, H. Calvert, Phase I and pharmacokinetic study of NC-6004, a new platinum entity of cisplatin-conjugated polymer forming micelles. *J. Clin. Oncol.* **26**, 2573 (2008).
18. R. Dent, M. Trudeau, K. I. Pritchard, W. M. Hanna, H. K. Kahn, C. A. Sawka, L. A. Lickley, E. Rawlinson, P. Sun, S. A. Narod, Triple-negative breast cancer: Clinical features and patterns of recurrence. *Clin. Cancer Res.* **13**, 4429–4434 (2007).
19. J. A. Hubbell, Materials science. Enhancing drug function. *Science* **300**, 595–596 (2003).
20. T. Minko, P. Kopecková, J. Kopecek, Efficacy of the chemotherapeutic action of HPMA copolymer-bound doxorubicin in a solid tumor model of ovarian carcinoma. *Int. J. Cancer* **86**, 108–117 (2000).
21. D. Kim, E. S. Lee, K. T. Oh, Z. G. Gao, Y. H. Bae, Doxorubicin-loaded polymeric micelle overcomes multidrug resistance of cancer by double-targeting folate receptor and early endosomal pH. *Small* **4**, 2043–2050 (2008).
22. K. Cho, X. Wang, S. Nie, Z. G. Chen, D. M. Shin, Therapeutic nanoparticles for drug delivery in cancer. *Clin. Cancer Res.* **14**, 1310–1316 (2008).
23. H. Cabral, N. Nishiyama, S. Okazaki, H. Koyama, K. Kataoka, Preparation and biological properties of dichloro(1,2-diaminocyclohexane)platinum(II) (DACHPt)-loaded polymeric micelles. *J. Control. Release* **101**, 223–232 (2005).
24. H. Cabral, N. Nishiyama, K. Kataoka, Optimization of (1,2-diamino-cyclohexane)platinum(II)-loaded polymeric micelles directed to improved tumor targeting and enhanced antitumor activity. *J. Control. Release* **121**, 146–155 (2007).
25. N. D. Sonawane, J. R. Thiagarajah, A. S. Verkman, Chloride concentration in endosomes measured using a ratioable fluorescent Cl^- indicator: Evidence for chloride accumulation during acidification. *J. Biol. Chem.* **277**, 5506–5513 (2002).
26. N. Nishiyama, F. Koizumi, S. Okazaki, Y. Matsumura, K. Nishio, K. Kataoka, Differential gene expression profile between PC-14 cells treated with free cisplatin and cisplatin-incorporated polymeric micelles. *Bioconjug. Chem.* **14**, 449–457 (2003).
27. I. D. Johnson, H. C. Kang, R. P. Haugland, Fluorescent membrane probes incorporating dipyrrometheneboron difluoride fluorophores. *Anal. Biochem.* **198**, 228–237 (1991).
28. S. Arnould, I. Hennebelle, P. Canal, R. Bugat, S. Guichard, Cellular determinants of oxaliplatin sensitivity in colon cancer cell lines. *Eur. J. Cancer* **39**, 112–119 (2003).
29. L. Kelland, The resurgence of platinum-based cancer chemotherapy. *Nat. Rev. Cancer* **7**, 573–584 (2007).
30. E. Raymond, S. Faivre, S. Chaney, J. Woynarowski, E. Cvitkovic, Cellular and molecular pharmacology of oxaliplatin. *Mol. Cancer Ther.* **1**, 227–235 (2002).
31. F. R. Luo, T. Y. Yen, S. D. Wyrick, S. G. Chaney, High-performance liquid chromatographic separation of the biotransformation products of oxaliplatin. *J. Chromatogr. B Biomed. Sci. Appl.* **724**, 345–356 (1999).
32. F. R. Luo, S. D. Wyrick, S. G. Chaney, Biotransformations of oxaliplatin in rat blood in vitro. *J. Biochem. Mol. Toxicol.* **13**, 159–169 (1999).
33. R. Duncan, Polymer conjugates as anticancer nanomedicines. *Nat. Rev. Cancer* **6**, 688–701 (2006).
34. T. Yamori, A. Matsunaga, S. Sato, K. Yamazaki, A. Komi, K. Ishizu, I. Mita, H. Edatsugi, Y. Matsuba, K. Takezawa, O. Nakanishi, H. Kohno, Y. Nakajima, H. Komatsu, T. Andoh, T. Tsuruo, Potent antitumor activity of MS-247, a novel DNA minor groove binder, evaluated by an *in vitro* and *in vivo* human cancer cell line panel. *Cancer Res.* **59**, 4042–4049 (1999).
35. S. Yaguchi, Y. Fukui, I. Koshimizu, H. Yoshimi, T. Matsuno, H. Gouda, S. Hirono, K. Yamazaki, T. Yamori, Antitumor activity of ZSTK474, a new phosphatidylinositol 3-kinase inhibitor. *J. Natl. Cancer Inst.* **98**, 545–556 (2006).
36. A. Vekris, D. Meynard, M. C. Haaz, M. Bayssas, J. Bonnet, J. Robert, Molecular determinants of the cytotoxicity of platinum compounds: The contribution of *in silico* research. *Cancer Res.* **64**, 356–362 (2004).
37. S. L. Kelley, A. Basu, B. A. Teicher, M. P. Hacker, D. H. Hamer, J. S. Lazo, Overexpression of metallothionein confers resistance to anticancer drugs. *Science* **241**, 1813–1815 (1988).
38. J. Holford, P. J. Beale, F. E. Boxall, S. Y. Sharp, L. R. Kelland, Mechanisms of drug resistance to the platinum complex ZD0473 in ovarian cancer cell lines. *Eur. J. Cancer* **36**, 1984–1990 (2000).
39. P. M. Deegan, I. S. Pratt, M. P. Ryan, The nephrotoxicity, cytotoxicity and renal handling of a cisplatin-methionine complex in male Wistar rats. *Toxicology* **89**, 1–14 (1994).
40. R. M. Goldberg, D. J. Sargent, R. F. Morton, C. S. Fuchs, R. K. Ramanathan, S. K. Williamson, B. P. Findlay, H. C. Pitot, S. R. Alberts, A randomized controlled trial of fluorouracil plus leucovorin, irinotecan, and oxaliplatin combinations in patients with previously untreated metastatic colorectal cancer. *J. Clin. Oncol.* **22**, 23–30 (2004).
41. D. Wang, S. J. Lippard, Cellular processing of platinum anticancer drugs. *Nat. Rev. Drug Discov.* **4**, 307–320 (2005).
42. I. Pastan, M. M. Gottesman, K. Ueda, E. Lovelace, A. V. Rutherford, M. C. Willingham, A retrovirus carrying an *MDR1* cDNA confers multidrug resistance and polarized expression of P-glycoprotein in MDCK cells. *Proc. Natl. Acad. Sci. U.S.A.* **85**, 4486–4490 (1988).
43. R. K. Jain, Delivery of molecular and cellular medicine to solid tumors. *Adv. Drug Deliv. Rev.* **46**, 149–168 (2001).
44. Y. Saito, M. Yasunaga, J. Kuroda, Y. Koga, Y. Matsumura, Antitumour activity of NK012, SN-38-incorporating polymeric micelles, in hypovascular orthotopic pancreatic tumour. *Eur. J. Cancer* **46**, 650–658 (2010).
45. M. Mishima, G. Samimi, A. Kondo, X. Lin, S. B. Howell, The cellular pharmacology of oxaliplatin resistance. *Eur. J. Cancer* **38**, 1405–1412 (2002).

46. Y. Akiyama, Y. Nagasaki, K. Kataoka, Synthesis of heterotelechelic poly(ethylene glycol) derivatives having α-benzaldehyde and ω-pyridyl disulfide groups by ring opening polymerization of ethylene oxide using 4-(diethoxymethyl)benzyl alkoxide as a novel initiator. *Bioconjug. Chem.* **15**, 424–427 (2004).
47. N. Nishiyama, S. Okazaki, H. Cabral, M. Miyamoto, Y. Kato, Y. Sugiyama, K. Nishio, Y. Matsumura, K. Kataoka, Novel cisplatin-incorporated polymeric micelles can eradicate solid tumors in mice. *Cancer Res.* **63**, 8977–8983 (2003).
48. W. H. Daly, D. Poche, The preparation of N-carboxyanhydrides of α-amino acids using bis(trichloromethyl)carbonate. *Tetrahedron Lett.* **29**, 5859–5862 (1988).
49. Y. Matsumoto, T. Nomoto, H. Cabral, Y. Matsumoto, S. Watanabe, R. J. Christie, K. Miyata, M. Oba, T. Ogura, Y. Yamasaki, N. Nishiyama, T. Yamasoba, K. Kataoka, Direct and instantaneous observation of intravenously injected substances using intravital confocal micro-videography. *Biomed. Opt. Express* **1**, 1209–1216 (2010).
50. **Acknowledgments:** M.M. thanks J. Ghaugas for his support and suggestions for preparing the manuscript and S. Hiro for his help with in silico data analysis. **Funding:** This research was supported in part by Funding Program for World-Leading Innovative R&D on Science and Technology (FIRST Program) from the Japan Society for the Promotion of Science (JSPS) and the Core Research Program for Evolutional Science and Technology (CREST) from the Japan Science and Technology Agency (JST). **Author contributions:** M.M. and H.C. designed and performed the experiments, analyzed the results, and wrote the manuscript. Y.M. performed the imaging experiments. S.W. performed the siRNA knockdown studies. T.Y. conducted human cell panel analysis. M.R.K. edited the manuscript. N.N. supervised the project and wrote the manuscript. K.K. supervised the project and edited the manuscript. **Competing interests:** The authors declare that they have no competing interests.

Submitted 14 June 2010
Accepted 10 December 2010
Published 5 January 2011
10.1126/scitranslmed.3001385

Citation: M. Murakami, H. Cabral, Y. Matsumoto, S. Wu, M. R. Kano, T. Yamori, N. Nishiyama, K. Kataoka, Improving drug potency and efficacy by nanocarrier-mediated subcellular targeting. *Sci. Transl. Med.* **3**, 64ra2 (2011).

Nonmyelinating Schwann Cells Maintain Hematopoietic Stem Cell Hibernation in the Bone Marrow Niche

Satoshi Yamazaki,[1] Hideo Ema,[2] Göran Karlsson,[3] Tomoyuki Yamaguchi,[1,2] Hiroyuki Miyoshi,[4,8] Seiji Shioda,[5] Makoto M. Taketo,[4] Stefan Karlsson,[3] Atsushi Iwama,[6,7] and Hiromitsu Nakauchi[1,2,*]

[1]Japan Science and Technology Agency, ERATO, Chiyoda-ku, Tokyo 102-0075, Japan

[2]Division of Stem Cell Therapy, Center for Stem Cell Biology and Medicine, Institute of Medical Science, University of Tokyo, Tokyo 108-8639, Japan

[3]Department of Molecular Medicine and Gene Therapy, Lund Stem Cell Center, Lund University Hospital, BMC A12, 221 84 Lund, Sweden

[4]Department of Pharmacology, Graduate School of Medicine, Kyoto University, Kyoto 606-8501, Japan

[5]Department of Anatomy, Showa University School of Medicine, 1-5-8 Hatanodai, Shinagawa-ku, Tokyo 142-8555, Japan

[6]CREST, Sanbancho, Chiyoda-ku, Tokyo 102-0075, Japan

[7]Department of Cellular and Molecular Medicine, Graduate School of Medicine, Chiba University, Chiba 260-8670, Japan

[8]Present address: Department of Pathology & Immunology, Washington University School of Medicine, St. Louis, MO 63110, USA

*Correspondence: nakauchi@ims.u-tokyo.ac.jp

DOI 10.1016/j.cell.2011.09.053

SUMMARY

Hematopoietic stem cells (HSCs) reside and self-renew in the bone marrow (BM) niche. Overall, the signaling that regulates stem cell dormancy in the HSC niche remains controversial. Here, we demonstrate that TGF-β type II receptor-deficient HSCs show low-level Smad activation and impaired long-term repopulating activity, underlining the critical role of TGF-β/Smad signaling in HSC maintenance. TGF-β is produced as a latent form by a variety of cells, so we searched for those that express activator molecules for latent TGF-β. Nonmyelinating Schwann cells in BM proved responsible for activation. These glial cells ensheathed autonomic nerves, expressed HSC niche factor genes, and were in contact with a substantial proportion of HSCs. Autonomic nerve denervation reduced the number of these active TGF-β-producing cells and led to rapid loss of HSCs from BM. We propose that glial cells are components of a BM niche and maintain HSC hibernation by regulating activation of latent TGF-β.

INTRODUCTION

Self-renewal, differentiation, and the cell cycle of hematopoietic stem cells (HSCs) are thought to be regulated by the signals provided by specific niches in bone marrow (BM). Many different cell types have been characterized as contributors to the formation of HSC niches, such as osteoblasts (Zhang et al., 2003; Calvi et al., 2003; Arai et al., 2004), endothelial cells (Kiel et al., 2005), chemokine (C-X-C motif) ligand 12 (CXCL12)-abundant reticular (CAR) cells (Sugiyama et al., 2006), and mesenchymal stem cells (MSCs) (Méndez-Ferrer et al., 2010). These cells are believed to provide microenvironments for HSC self-renewal, differentiation, mobilization, and hibernation by cell-to-cell contact and soluble factors, including angiopoietin-1 (Ang-1) (Arai et al., 2004), Ca^{2+} ions, CXCL12, sonic hedgehog, osteopontin, stem cell factor (SCF), and thrombopoietin (TPO). Contributions by as yet unidentified cells and factors have also been speculated (Kiel and Morrison, 2008).

Most HSCs in the BM niche are in a hibernating state from which they are occasionally aroused to undergo cell division on average every 1–2 months (Sudo et al., 2000; Foudi et al., 2009; Bradford et al., 1997; Cheshier et al., 1999). We recently demonstrated that lipid raft clustering is a key event in the regulation of HSC hibernation (Yamazaki et al., 2006). Lipid raft clustering, as induced by cytokines, augmented signals that appeared essential for HSC entry into the cell cycle. Conversely ex vivo, inhibition of lipid raft clustering caused sustained nuclear accumulation of FoxO transcription factors and induced HSC hibernation. These findings established a critical role for lipid rafts in regulating the cell cycle, survival, and apoptosis of HSCs and uncovered a striking similarity between HSC hibernation and *C. elegans* dauer formation.

We hypothesized that a niche factor regulates the lipid raft clustering of HSCs in vivo. Screening of candidate niche signals revealed that transforming growth factor β (TGF-β) efficiently inhibited cytokine-mediated lipid raft clustering and induced HSC hibernation ex vivo, establishing TGF-β as a candidate niche signal in the control of HSC dormancy (Yamazaki et al., 2009). TGF-β negatively regulates HSC and hematopoietic progenitor cell proliferation in vitro (Larsson and Karlsson, 2005). TGF-βs are secreted as part of the large latent complex (LLC) consisting of TGF-β, latency-associated protein (LAP), and latent TGF-β binding protein-1 (LTBP-1) (Annes et al., 2003). Because LTBP-1, a member of the LTBP/fibrillin family, covalently binds to extracellular matrix (ECM) proteins, the LLC accumulates in the ECM (Annes et al., 2003). Under most conditions TGF-β in the LLC is inactive and is thus called latent TGF-β.

Therefore, TGF-β function is largely controlled by activation of latent TGF-β, a process that involves dissociation of bioactive TGF-β from LAP. As such, we further hypothesized that cells that activate latent TGF-β were a component of the BM HSC niche and sought them in BM. Glial fibrillary acidic protein (GFAP)-expressing cells ("glial cells") were unexpectedly identified as the cells that principally process latent TGF-β into active TGF-β in BM. These GFAP-positive cells were nonmyelinating Schwann cells, which ensheath sympathetic nerves in BM. They produced niche factors and were in direct contact with a significant proportion of HSCs. Most strikingly, autonomic nerve denervation of BM reduced the number of these TGF-β secreting glial cells and led to the disappearance of $CD34^-KSL$ HSCs.

RESULTS

TGF-β/Smad Signaling Is Active in HSCs in BM

To ascertain how TGF-β controls hibernation of HSCs, we first generated lymphocyte-deficient conditional TGF-β type II receptor (TβRII)-deficient mice. TGF-β binds to its receptor composed of TβRII and TGF-β type I receptor (TβRI) (Waite and Eng, 2003; Schmierer and Hill, 2007). TGF-βs are multipotent cytokines that modulate cell growth, inflammation, matrix synthesis, and apoptosis (Waite and Eng, 2003; Schmierer and Hill, 2007), and *Tgfb1* null mice develop a lethal inflammatory disorder (LID) affecting multiple organs that is caused by uncontrollable overreaction of lymphocytes. Similarly, immune cells from *Tgfbr2* knockout mice should induce LID upon transplantation. Therefore, we generated *Mx-1-Cre*:$Tgfbr2^{flox/-}$:$Rag2^{-/-}$ mice by crossing $Tgfbr2^{+/-}$ mice (Oshima et al., 1996), $Tgfbr2^{flox/+}$ mice (Levéen et al., 2005), $Rag2^{-/-}$ mice, and interferon-inducible *Mx-1-Cre* transgenic mice. To induce *Cre*, polyinosinic-polycytidylic acid (pIpC) was injected intraperitoneally three times every other day. *Mx-1-Cre*:$Tgfbr2^{flox/-}$:$Rag2^{-/-}$ mice lacking T and B lymphocytes did not develop LID. Two weeks after pIpC injection, total BM cells from *Mx-1-Cre*:$Tgfbr2^{+/-}$:$Rag2^{-/-}$ mice or *Mx-1-Cre*:$Tgfbr2^{flox/-}$:$Rag2^{-/-}$ mice (B6-Ly5.1) were infused into lethally irradiated recipients (B6-Ly5.2) along with the same number of BM competitor cells from B6-Ly5.1xLy5.2 F1 mice. The repopulation capacity of test cells was monitored in terms of peripheral blood (PB) chimerism (Figure 1A). Because $Rag2^{-/-}$ cells do not give rise to B and T cells, only myeloid cells were gated upon analysis. The contribution of $Tgfbr2^{del/-}Rag2^{-/-}$ BM cells to PB myeloid cells gradually declined over time (Figure 1B).

After binding to its ligand, the activated TGF-β receptor complex subsequently phosphorylates receptor-activated Smads (R-Smads) 2 and 3. R-Smads eventually heterodimerize with the common mediator Smad4. The resulting ternary complex translocates to the nucleus, where it recruits transcriptional cofactors to control expression of genes, including those involved in the cell cycle (Larsson and Karlsson, 2005; Waite and Eng, 2003; Schmierer and Hill, 2007). Immunostaining in wild-type BM sections revealed that a high proportion of BM cells expressed phosphorylated Smad2/3 (Figure 1C). Smad2/3 have been shown to be activated broadly among different developmental stages of hematopoietic cells. Among members of the TGF-β family, Nodal and Activin are known to phosphorylate Smad2/3 (Larsson and Karlsson, 2005). Although T cells can respond to both Activin and TGF-β (Rosendahl et al., 2003), we have shown that HSCs do not respond to Activin or Nodal (Yamazaki et al., 2009). To evaluate pSmad2/3 status within HSCs, BM sections were stained with anti-CD150, -CD48, -CD41, and -lineage marker antibodies (Kiel et al., 2005) and analyzed using ArrayScan technology (see Figure S1 available online). ArrayScan can quantitatively analyze BM histological sections containing large numbers of cells (Figure S1A) and can backtrack the location and phosphorylation status of individual very rare $CD150^+CD48^-CD41^-Lin^-$ HSCs (Figure 1D; Figure S1B; scattergram gated in a red square, and Figures S1C and S1D). We confirmed that these HSCs were phosphorylated with Smad2/3 in a fashion similar to that in freshly isolated wild-type $CD34^-KSL$ HSCs as previously observed (Figure 1D) (Yamazaki et al., 2009).

We then examined the phosphorylation status of Smad2 and Smad3 in $Tgfbr2^{del/-}Rag2^{-/-}$ $CD34^-KSL$ HSCs 2 weeks after pIpC injection. As expected, the levels of pSmad2/3 were significantly lower than those in $Tgfbr2^{+/+}Rag2^{-/-}$ $CD34^-KSL$ HSCs (Figure 1E). In parallel with the reduction in p-Smad2/3 expression, a significantly higher proportion of $Tgfbr2^{del/-}Rag2^{-/-}$ $CD34^-KSL$ HSCs entered the cell cycle within 1 week compared with $Tgfbr2^{+/-}Rag2^{-/-}$ HSCs, as determined by a bromodeoxyuridine (BrdU) incorporation assay (Figure 1F). Loss of *Tgfbr2* was associated with reduced p-Smad2/3, increased cycling, and reduced long-term repopulating activity in HSCs. These results demonstrated for the first time that TGF-β/Smad signaling is active in BM HSCs and maintains their dormancy.

A Specialized Cell Type Produces Active TGF-β in BM

TGF-β is produced by a variety of cells, including HSCs, in a latent form. However, HSCs cannot activate it by themselves (Yamazaki et al., 2009). We thought that it may be critical to identify cell types that can activate latent TGF-β in order to understand the physiological role of TGF-β in BM. To address this issue, we used two antibodies: anti-LAP antibody and anti-TGF-β antibody. Both LAP and TGF-β exist as disulfide-linked homodimers, and these molecules are noncovalently associated, forming the latent TGF-β complex. Anti-LAP antibody was used to detect latent TGF-β. Anti-TGF-β antibody reacts with TGF-β only after TGF-β is released from the latent TGF-β complex. Anti-TGF-β antibody was used to detect active TGF-β. Citric acid treatment can release TGF-β from the latent TGF-β complex (Lyons et al., 1990). The specificity of anti-TGF-β antibody was examined by ELISA. Anti-TGF-β antibody did not bind to TGF-β but bound to TGF-β after citric acid treatment (Figure S2A). As reported previously (Yamazaki et al., 2009), in vitro colony formation by $CD34^-KSL$ HSCs is inhibited by active TGF-β, but not by latent TGF-β. This colony formation inhibited by active TGF-β was completely rescued by addition of anti-TGF-β antibody, but not of anti-LAP antibody (Figure S2B). These results indicate that the anti-LAP antibody recognizes latent TGF-β in most cases and that anti-TGF-β antibody specifically recognizes active TGF-β.

Correspondingly, the two antibodies successfully unveiled differential patterns of expression of latent TGF-β and active

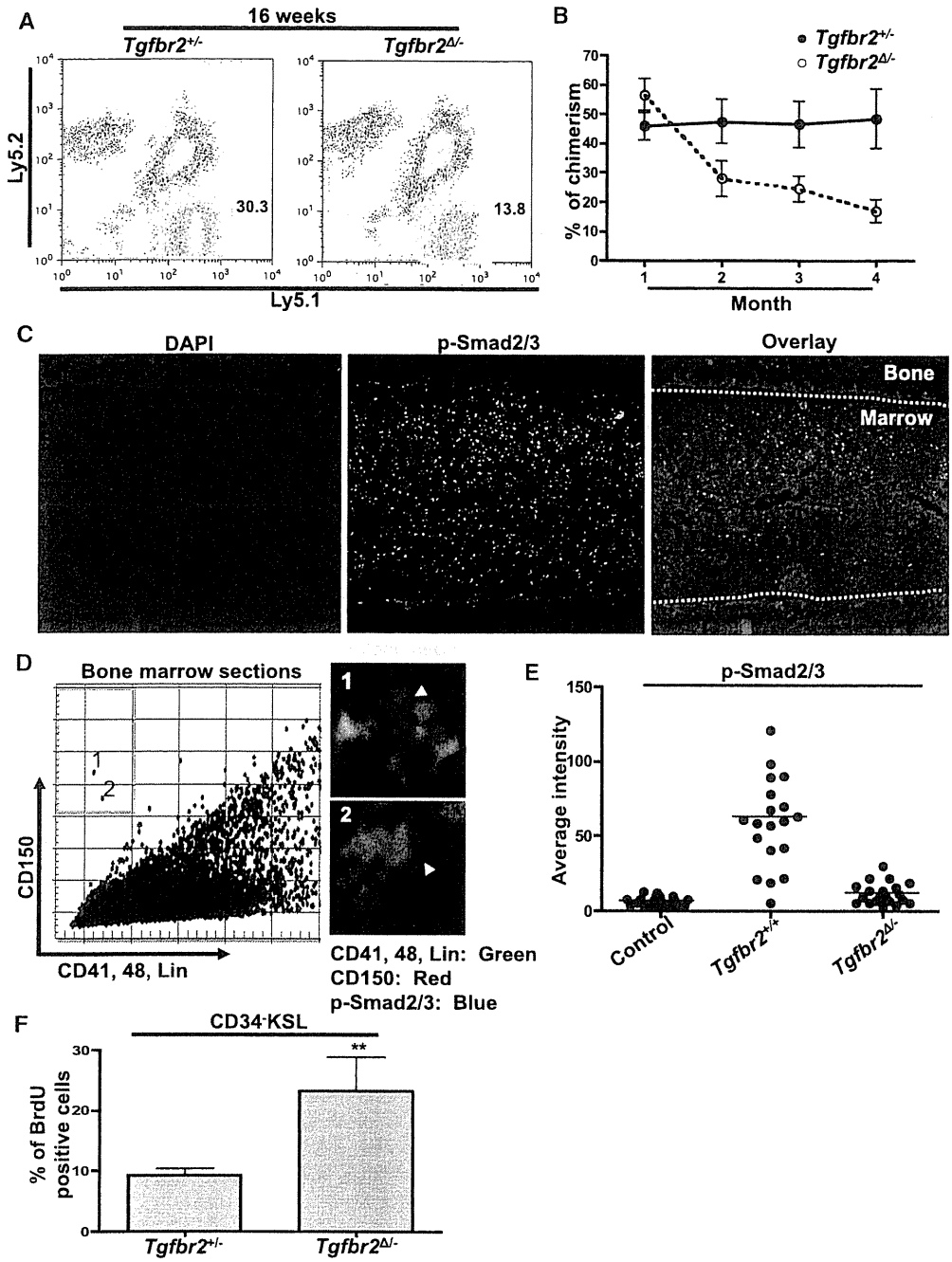

Figure 1. Impaired HSC Function, Decreased Smad2/3 Phosphorylation, and Increased Cell Cycling in *Tgfbr2*-Deficient Mice

(A) Contribution of $Tgfbr2^{+/-}Rag2^{-/-}$ or $Tgfbr2^{del/-}Rag2^{-/-}$ cells to hematopoiesis detected 16 weeks after transplantation. Competitive repopulation assays were performed using 1 × 10^6 BM cells from $Tgfbr2^{+/-}Rag2^{-/-}$ mice or $Tgfbr2^{del/-}Rag2^{-/-}$ mice (B6-Ly5.1) and the same number of BM competitor cells from F1 mice (B6-Ly5.1/5.2). Cells were transplanted into lethally irradiated B6-Ly5.2 mice. The repopulation capacity of test cells was monitored in terms of PB chimerism of myeloid cells (n = 10).

(B) Time course analysis of chimerism. Chimerism for donor-derived cells was periodically analyzed in PB myeloid cells. Data are presented as mean ± SD (n = 10).

(C) Phosphorylation status of Smad2 and Smad3 in wild-type BM as detected by immunostaining of frozen BM sections with DAPI (blue) and anti-p-Smad2/3 (green).

(D) Two-dimensional presentation of wild-type BM section data automatically assayed by ArrayScan. Frozen BM sections were stained with antibodies against CD150 (red), against CD48, CD41, and lineage markers (green), and against pSmad2/3 (blue). Gated cells in a red square represent $CD150^+CD48^-CD41^-Lin^-$ HSCs. Fluorescence photomicrographs show pSmad2/3 in $CD150^+CD48^-CD41^-Lin^-$ HSCs within the red square. A magnified image of smad2/3-positive hematopoietic stem cells (arrowheads). See also Figure S1.